Mechanical (and Materials) Engineering -- Dissertations, Theses, and Student Research

Mechanical & Materials Engineering, Department of

5-2018

# Peridynamic Modeling of Dynamic Fracture in Bio-Inspired Structures for High Velocity Impacts

Sneha Akula

*University of Nebraska-Lincoln*, snehaakula1993@gmail.com

PERIDYNAMIC MODELING OF DYNAMIC FRACTURE IN BIO-INSPIRED

STRUCTURES FOR HIGH VELOCITY IMPACTS

by

Sneha Akula

A THESIS

Presented to the Faculty of

The Graduate College at the University of Nebraska

In Partial Fulfillment of Requirements

For the Degree of Master of Science

Major: Mechanical and Materials Engineering

Under the supervision of Professor Florin Bobaru

Lincoln, Nebraska

May 2018

PERIDYNAMIC MODELING OF DYNAMIC FRACTURE IN BIO-INSPIRED

STRUCTURES FOR HIGH VELOCITY IMPACTS

Sneha Akula, M.S

University of Nebraska, 2018

Advisor: Florin Bobaru

Bio-inspired damage resistant models have distinct patterns like brick-mortar, Voronoi, helicoidal *etc*., which show exceptional damage mitigation against high-velocity impacts. These unique patterns increase damage resistance (in some cases up to 3000 times more than the constituent materials) by effectively dispersing the stress waves produced by the impact. Ability to mimic these structures on a larger scale can be ground-breaking and could be used in numerous applications. Advancements in 3D printing have now made possible fabrication of these patterns with ease and at a low cost. Research on dynamic fracture in bio-inspired structures is very limited but it is crucial for the development of such materials with enhanced impact resistance.

In this thesis, we investigate damage in some bio-inspired structures through peridynamic modeling. We first print a 3D brick-mortar structure, 82% VeroClear plastic (a PMMA substitute in 3D printing; the stiff phase) and 18% TangoBlack rubber (a natural rubber substitute in 3D printing; the soft phase). We investigate damage in this 3D printed sample by low-velocity drop test with fixed and free boundary conditions.

Under free boundary conditions, at this impact speed no damage was observed, while cracks form when the sample rests on a fixed metal table.

A 3D peridynamic model for dynamic brittle fracture is used to first validate it against the Kalthoff-Winkler experiment, in which a pre-notched steel plate is impacted at 32m/s by a cylindrical impactor and brittle cracks grow at a 70-degree angle with the impact direction. A new peridynamic model for a brick-mortar microstructure is created using the properties of PMMA and rubber. Because simulating the supporting table used in the experiments would be too costly, we choose to work with free boundary conditions and a higher impact speed (500m/s), to observe damage in the peridynamic model of the brick-mortar structure. Under these conditions, the damage is limited to the contacting brick only. The soft phase is able to limit its spread. Other boundary conditions are likely to cause wave reflections and reinforcements, which can damage other bricks, far from the impact point, as observed in our experiments.

# AUTHOR'S ACKNOWLEDGEMENTS

# CONTENTS

# TABLE OF FIGURES

# CHAPTER 1: INTRODUCTION

The introduction chapter includes motivation for thesis, a brief review of bio-mimicry & bio-mimetics their advantages and challenges for large-scale manufacturing. Next, we discuss damage tolerance in materials and objectives of thesis regarding expected advancements by bio-mimicry. Lastly, we study challenges of manufacturing bio-inspired materials and new advancements in technology to address the challenges.

## 1.1 Inspiration and motivation – Bio-mimicry

Bio-mimicry is an inspiration for numerous engineering designs and mechanisms in the world. Many technologies have adapted mechanisms and shapes from nature to improve their performance. Studying how each component contributes to the overall material properties in micro and meso scales enables us to design better structures. Most famous examples of biomimicry include Bullet train's front end design based on Kingfisher beak, prosthetic arms based on tentacles for handicapped and agriculture field patterns inspired by prairies for sustainable farming[1]. In particular, Biomimetics deals with the synthesis of novel materials, devices, and structures by studying the building blocks of microstructures to understand their effect on overall properties of the structures.

Damage tolerant structures consist of building blocks in unique stacking and patterns which impart some extraordinary properties to them. For example in nacre, the mother of pearl, 5% inclusion of soft bio-polymer increases its toughness by 3000 times compared to its constituent materials.

There is extensive research on how the building blocks lead to material hierarchy, morphing, interlocking for bio-inspired structures in [2] and [3], where many structures like gecko feet, hydrophobic lotus leaves, bone matter are discussed in depth. Despite the fascinating behaviors in many organisms, there are limited applications of biomimetics in engineering. This is because fabrication of the complex patterns of the bio-inspired structures is tedious and expensive. Advancements in additive manufacturing processes like binder jetting and polymer jetting (which can print multiple materials at a very fine resolution) have paved new possibilities. With 3D printing, bio-inspired structures can be built with ease, this led to a renewed focus on bio-inspired structures.

## 1.2 Damage Resistant Structures

Damage resistance/tolerance of a material is the ability to withstand damage while maintaining its structural rigidity. Damage resistant structures are extremely important in high-velocity impact applications like bulletproof vests, energy storage containers and projectile proof buildings. Usually, strength and toughness are the material properties which are available exclusively in nature. For example, metals have high toughness but have low yield strengths compared to ceramics, while ceramics cannot sustain strain and get damaged by brittle fracture. With bio-inspired composites, we can achieve best of both ceramics and metals by mimicking basic building blocks of the materials (

Figure **1**). This is done by studying the building blocks of a microstructure and implementing it by additive manufacturing process for required properties.

Materials which are both tough and strong can be found in nature with very good damage tolerance, they disperse the stress waves imparted through impact with their microstructures [4]. In particular, nacre shell's microstructure consists of aragonite ($CaCo_3$, 95% volume) combined with a softer organic biopolymer (5% volume) in brick-mortar pattern (Figure 2). This pattern makes the nacre 3000 times stronger than aragonite and disperses the impact wave which is pretty impressive [5]. A similar fascinating phenomenon is seen in stomatopods, Figure 2. These are small marine creatures which use hammer-like claws to break open hard shells of their prey and to attack the enemies. The hammer-like claws also called dactyl clubs deliver high-velocity impacts repeatedly with forces greater than 700 N.
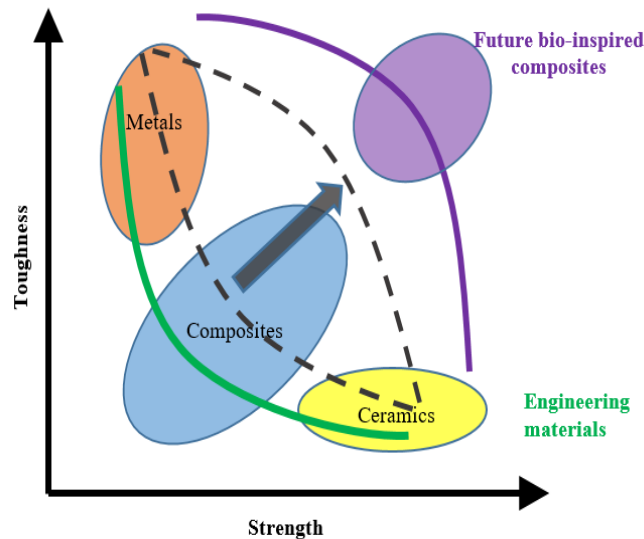


**Figure 1** Schematic representation of the bio-inspired composites having both strength and toughness of composites and metals

Their prey consists of mollusk shells, crab exoskeletons, and skulls of small fish which are biologically damage-tolerant materials. Stomatopod's ability to break shells without damaging itself prompted many studies regarding its internal microstructure. The microstructure enables absorption of the high-speed impacts and makes it extremely damage-tolerant [6]. Similar is the case with mollusk shell [7], it's microstructure has inclined platelets, which impart very good damage tolerance to the shells. The microstructures of these organisms effectively disperse the stress waves from impact minimizing the damage to the structures [8].

These microstructures consist of complex minerals and brittle phases stacked in unique patterns and orientations which give them extraordinary damage tolerant properties. Brittle phases have soft phases or gaps in intricate patterns which evolved over millions of years to sustain the environment. Although the properties of the organisms depend on various factors such as hydration, size, and orientation [4].



(a)     (b)     (c)
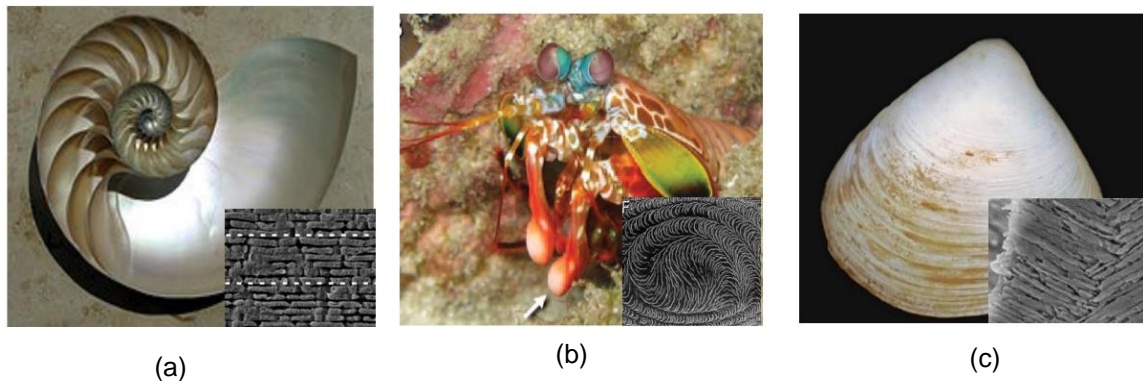
**Figure 2** Damage tolerant organisms with their microstructures in the inset images. (a) Nacre's brick-mortar pattern [9]. (b) Stomatopod Dactyl club's helicoidal pattern [6]. (c) Mollusk Shell's inclined platelets pattern [7].

Successful mimicking of such microstructures will enable development of highly damage tolerant materials which can be used in high-velocity impact applications, such as spacecraft liners, armored vehicles and, projectile proof buildings. We selected brick-mortar pattern because it is the simplest structure to study and is found in highly damage tolerant mollusk shell and nacre.

## 1.3    Fabrication of Bio-inspired structures

Traditionally following methods have been used to manufacture these bio-inspired patterns. Those include ice-templating, compositing layers of thin films, creating microfibers using optical lithography, polymer micro molding and reactive spark plasma sintering [2, 10-14]. Most of the processes are nano-scale processes used for stacking and developing chemical bonds between the layers. These processes are difficult and expensive for large-scale production. To overcome this rather than developing a material which has these microstructures in a micro-scale, magnified patterns at meso-scales can be fabricated by 3D printing.

Grace *et al.* [12] improvised an approach to have mesoscale bio-inspired structures rather than traditional micro-scale structures to mitigate cracks while retaining its structural rigidity. Some noted mesoscale structures such as brick-mortar of nacre, honeycomb, hourglass shapes comprising normally 2/3 materials printed by 3D printing. These structures were tested for their behavior in quasi-static loading conditions for their structural rigidity. Quite some research is available on quasi-static loading but research on dynamic testing for bio-inspired structures of 3D printing is very limited.

Even though there are some dynamic tests for the hardness of the structures [15] they are not applicable to high strain rate applications. In cases where dynamic testing is computed numerically [5, 16], the focus is mainly on delamination of the soft phase. Hence the study of damage in high strain rate applications for 3D printed structures is not available and is crucial for the development of materials with enhanced impact resistance.

For developing damage tolerant microstructures, brick-mortar, Voronoi and helical patterns could be considered for inspiration. These microstructures are known for their damage tolerance and wave dispersion mechanisms. Impact resistance of these patterns can be investigated aptly by the dynamic loading experiments. Even though there is an improvement in quasi-static applications with bio-inspired structures [12, 17-19], dynamic impact loading is where these structures have exceptional properties.

Simplest microstructure is brick-mortar and was selected as initial microstructure for analysis. The nacre having brick-mortar structure has CaCO3 and soft-biopolymers as its constituent materials. These are referred to as a stiff and soft phase of the microstructure. The soft phase consists of 5% of the total volume of the microstructure. To analyze the brick-mortar pattern approximately 80% volume ratio would be ideal for computations.

Brick-mortar pattern is first printed with 82% VeroClear plastic (a PMMA substitute, the stiff phase) and 18% TangoBlack rubber (a natural rubber substitute, the soft phase) by a polyjet printer. Damage in the 3D printed sample is investigated by low-velocity drop test experiments with fixed and free boundary conditions. [ refer section: 3.3].

For computations of the brick-mortar pattern a 3D peridynamic model for dynamic brittle fracture is modeled.  First 3D peridynamic code is validated against Kalthoff-Winker experiment [ refer to section 5.1]. And after validation of the model, convergence studies are performed to determine the peridynamic properties for the brick-mortar model. Then the damage in brick-mortar models with safe stiff-soft volume ratio is studied.

**CHAPTER 2: LITERATURE REVIEW**

In the literature review chapter, we discuss what different methods are available for development of damage tolerant materials other than bio-mimicry. Then we review different microstructures and manufacturing methods available for the bio-inspired structures. After reviewing the fabrication processes, we discuss existing research on the bio-inspired structures for both quasi-static and dynamic loading conditions.

**2.1    Literature review of Damage Tolerant materials by Optimization**

In literature, the damage tolerant structures are simulated by different topology and structural optimizations. In [20, 21] topology optimization is carried out by removing elements with an imposed constraint like large stress intensity factors and simulating the optimized structure. Organisms like stomatopod and nacre have microstructures that are called full stressed configurations and these parameters are used to create the patterns. In some cases, mimicking of these structures is attempted without a secondary material in the model. The absence of secondary material (soft phase) did not improve the existing structures when compared to bio-inspired structures.

Reference paper [22] depicts another way of achieving damage tolerant material. After impacting the sample, fractured or high-risk stiff material (a high ratio of tensile stress to strength) is replaced with soft phase within the volume constraints.

In other cases, soft phase is distributed randomly in the stiff phase initially and rearranged after iterations. Gradually replacing the material from the fracture zone to a soft material to finally achieve a damage tolerant structure is done as shown in Figure 3. This method was good at developing new micro-structures but computational cost is very high. It is also worth noting that the tests were done in quasistatic loading conditions meaning higher computational cost for dynamic impact loading simulations. A similar method proposed by James, and Waisman in [23],where initially the worst damage model is simulated and then topology optimization is carried out. The modification of structure is by adding the material rather than arranging the existing soft material as in the previous case. In this paper, it is worth noting that each case required a thousand iterations for each optimized structure. This does not necessarily guarantee the optimal damage tolerant structure because after the replacement of the soft phase the high-stress regions are re-distributed in the sample and have to be further investigated.
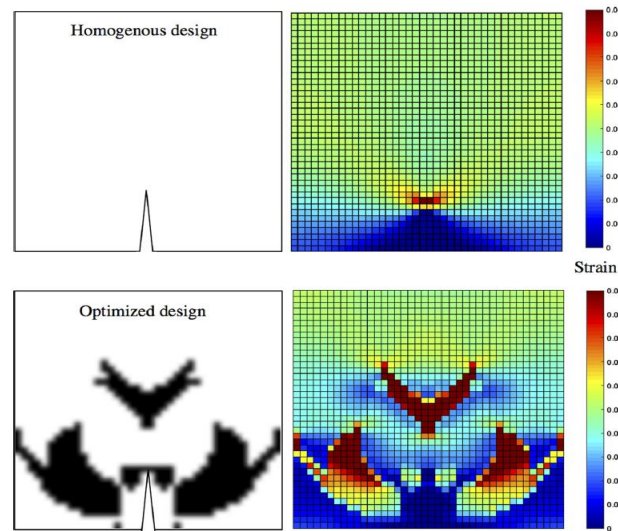


**Figure 3** Topology optimization Black material represents the soft phase and red represents the damaged / high-stress region [22]

**2.2 Types of building blocks for Micro-structures and previous research models**

All structures consist of basic building blocks, mimicking these building blocks of structures is crucial for bio-mimetics. In this section, we will review some microstructures of naturally damage-tolerant materials. First, we will discuss brick-mortar structure found in nacre, it filters and dissipates the waves incoming [24-26]. Quite a few papers have done simulations and experiments for brick-mortar pattern [11, 13, 15, 24] to study the quasi-static loading. In [16] the dynamic impact loading simulations are carried out for the brick-mortar structures, the damage is not localized and involves the impactor to penetrate the sample completely. This does not give us how the soft phase influences the damage. In [25], interface toughness of carbon epoxy fibers is studied. In most of the experiments, quasi-static tests were carried out but not the dynamic tests. Even in case of the dynamic impact tests damage was not localized and needs more insight.

Next, for the future studies, the following microstructures of the damage tolerant organisms have to be studied for the dynamic impact. The microstructure of mantis shrimp reveals helicoidal chitin fibers [6] in the impact region and spiral pattern in protecting region which dissipate the waves with no damage. In [18] semi helicoidal pattern was observed to give the most fracture mitigation as it mimics helically shaped fibers in stomatopod. The Voronoi structure is observed in abalone shells, and it would be interesting to study the effects of Voronoi patterns have on the dynamic fracture as the mollusk shells have very good damage tolerance. In case of mollusk shells [26] and [7], crisscross linking pattern of the microstructures.

Apart from the patterns in microstructure there are many other factors which influence impact resistance in a material. Factors such as volume ratio of soft phase to hard phase in the microstructure, aspect ratio of brick length to width in brick-mortar, percentage of moisture content, *etc*. [27] contribute to the impact resistance. 20% volume ratio for the soft phase to hard phase material to accommodate the computational cost of simulations. Effects of other parameters are to be considered for future studies.

As discussed above there are quite a few quasi-static experiments on bio-inspired patterns but no dynamic impact experiments at high strain rate loading. Because there were no dynamic impact loading tests to be validated against the computational tests we designed low-velocity drop tests to compare the results [ refer to section 3.3].



(a)                                                    (b)
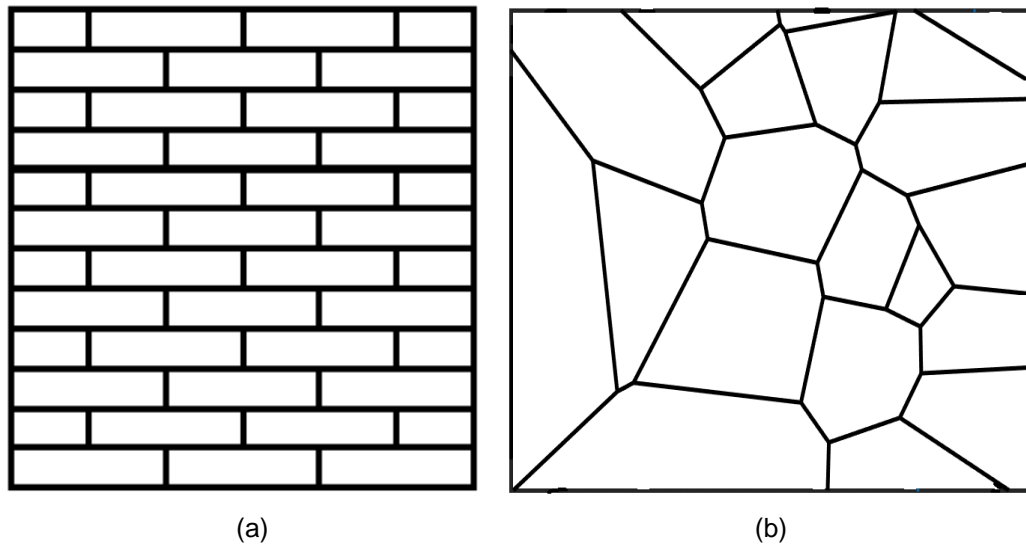
**Figure 4**  (a) Brick-mortar structure, (b) Voronoi patterned structure.

**2.3 Literature review of previous methods of fabrication for damage tolerant materials**

Traditionally some methods have been used to fabricate these patterns such as ice-templating, fabricating composite layers by thin films, creating microfibers using optical lithography, polymer micro molding and reactive spark plasma sintering [2, 10-12, 14, 28]. The main obstacle of these processes was the production of macroscale applications as most of them are nano-fabrication processes. Nano-fabrication processes used for stacking and developing chemical bonds between the ceramic layers is tedious and expensive.

In the past various ways of fabrication such as lamination of aragonite blocks [15] stacking of carbon fiber reinforced polymers in a helix shape [29], 3D printing ,freeze casting Figure 5 was used for the brick-mortar pattern. However, lamination and stacking cannot produce the microstructure on the same layer and freeze casting does not produce perfect micro-structure, see [30].  To overcome this rather than developing a material which has these microstructures in a micro-scale, magnified patterns in meso-scale can be fabricated easily by 3D printing.

In additive manufacturing processes (3D printing) there are 3 different ways to fabricate multi-material models. Namely, selective laser sintering powder bed fusion process (PBF), multi-extruder fused deposition modeling (FDM), and material jetting process. PBF process was used to print brick mortar structure by glass flakes and PLA binder [13]. As seen in Figure 5 micro-structure is not uniform and has big inclusions of the matrix thus cannot be ideal for testing.

The drawback of using the FDM process is that the materials available are very limited and bonding between the stiff and soft phases is not effective. The best process by which we can print these micro-structures with required precision and accuracy is by material jetting process [31]. Stratasys Objet Connex 500 is such polyjet printer where printer deposits the liquid photopolymer in droplets on the build platform, like the inkjet printing, and cures them with a UV light layer by layer.
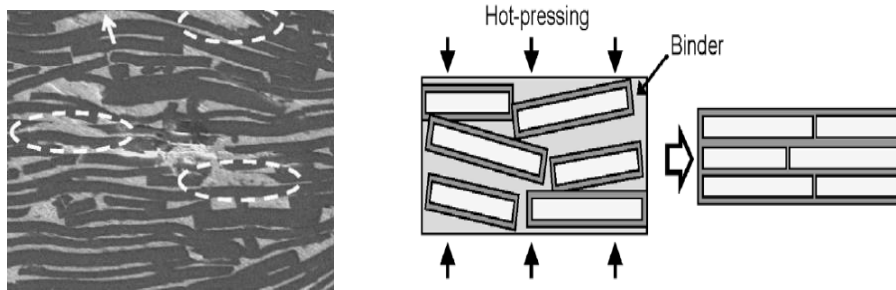


**Figure 5** Microstructure of the sample on the left and expected sample on the left by PBF process[13]

# CHAPTER 3: LOW-VELOCITY IMPACT TESTING OF BRICK-MORTAR STRUCTURES.

As discussed before we selected the type of microstructure and volume ration of soft to stiff phase in the microstructure. In this chapter, we will study the low-velocity impact experiments conducted. First, we select materials for printing of model. Then, basic principles of the additive manufacturing process are discussed along with the 3D printing process used for printing samples. Next, low-velocity impact experiments are studied to investigate the damage in the brick-mortar structures. The drop-test machine parameters, experimental setup and the results are discussed at the end of this chapter.

## 3.1 Material selection

For the brick-mortar model there are two materials. One is soft-phase (TangoBlackPlus rubber) and other is stiff phase (VeroClear plastic).

**Stiff phase:** As discussed in the previous chapter, polyjet printer is the best way to fabricate the experimental samples. Stratasys Objet Connex printer is highly credited due to its huge variety of material selection (120 materials including 100 digital materials). Among its materials, some of the stiff materials which can be considered for the model are grouped under rigid opaque and rigid transparent plastics. Transparent rigid plastics are a better choice as the cracks could be seen clearly. This plastic is named VeroClear plastic (RGD810) which is a photopolymer synthesized by Stratasys itself.

**Soft phase**: For the soft phase rubber-like compound called TangoBlackPlus (FLX980) from the Tango family is chosen as it is the softest rubber available for the printer and provides good contrast for the transparent plastic for deformation after the impact.

## 3.2 Additive Manufacturing Process

For any additive manufacturing process, there are 8 key steps listed below:

i) *CAD:* Creating of 3D model of the sample, this is done by Solid works software. Micro-structure (soft-phase) and stiff phase are designed as two different parts and assembled together.

ii) *.STL file conversion*: This step includes meshing of the 3D sample. This is done by crating surfaces from the co-ordinate points.

iii) *File transfer:* .STL file is to be imported to Objet software. In this step, we assign different materials to the model and determine its optimum positioning, orientation on the build tray (bed). The support structures are generated, then the software slices the Model into horizontal layers and sends it to the printer.

iv) *Machining set-up:* These include making sure the build tray is clean without any residual support material sticking from the previous jobs. This Printer automatically sets the header temperatures per the material selected or else manual input of the Bed and Nozzle temperature is to be given.

v) *Build*: Refers to the printing of the sample by the machine.

vi) *Removal:* Removal process is an important step of 3D printing as it may determine the efficiency of the whole part just by this step. Extreme care must be taken while removing the part from the bed as it may lead to bending of the sample, sticking of the sample to the bed, warping effect and excess melting of the initial layer due to elevated bed temperatures can be seen. In Objet Connex printer the support material surrounding the sample is a gel and is easily scraped off from the bed by the removal blade. This ensures all samples are removed in the same manner hence accounting for repeatability of the experiment.

vii)  *Post-Process:* In general, it refers to the removal of support structures, surface finish operations, heat treatment, laser shot peening processes *etc*., for different mechanisms to have required properties. For this experiment cleaning of the sample by speed water jet to completely remove the support structure is the only post-processing required.

viii) *Application:* 3D printed parts are sent for usage in this case for the dynamic testing of the sample.
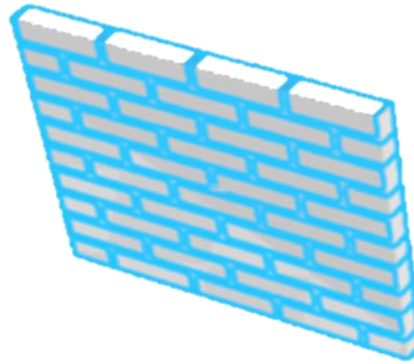
**Figure 6** Assembled Brick Mortar structure

**3.3 Polyjet Printing Process**

In this section, basic principles of the polyjet printer along with specifications of the Stratasys Objet Connex 500 polyjet printer are discussed. Polyjet printer is a Material Jetting process. According to fixed designation F2792 of ASTM definition of Material jetting is given as "material jetting, an additive manufacturing process in which droplets of build material are selectively deposited". Polymers are processed to be photoreactive liquids which when jetted on the bed can be cured by a light source, UV light in this case. In Figure 7 there is a Jetting Header which consists of around 6 model nozzles and 2 support material nozzles (not shown in Figure) from which droplets of material are jetted.

For our sample, we will be using 3 nozzle heads one for each soft phase, stiff phase and support materials. 3D printed part is coated on all sides with support material to ensure easy removal and even heat distribution throughout the sample. In the magnified part on the below-left corner of Figure 7, three materials can be seen with the imaginary depiction of layers in which they will be printed. The material jetting is in the 2D shape of the x-y cross-section of the sample enabling a fast processing time.

The jetter head moves in x and y directions as the bed support moves in the z-direction for every layer deposited. The jetter head moves depositing droplets and simultaneously curing them with UV light. In [32]it is depicted how the placement of the polyjet printed parts is affected by the orientation and placement of the sample on the build tray changes the properties of the samples printed. Hence the parts are printed at the same location to avoid any discrepancies due to printing.
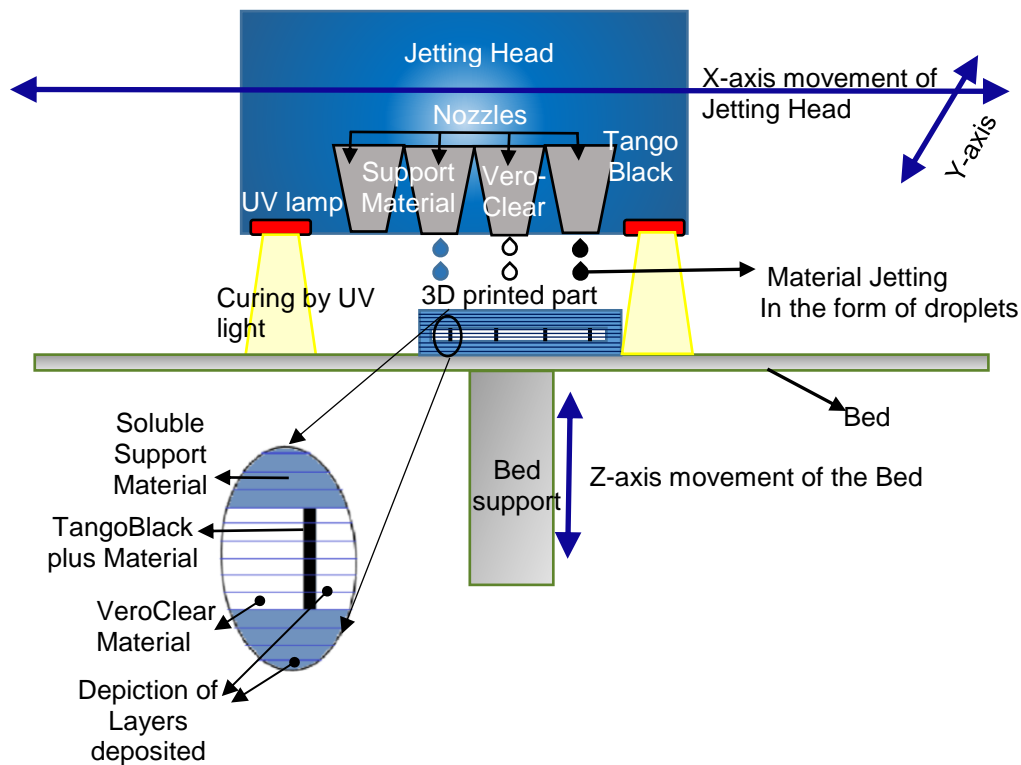
**Figure 7** Basic principles of Stratasys Objet Connex 500 printer

Stratasys Objet Connex 500:

After the first commercialization of the 3D printing by the 3D systems in 1988 of

the Stereolithography (SLA) process, Stratasys introduced the FDM process in 1989 by

S. Scott Crump and Lisa Crump. The Stratasys Objet Connex 500 was introduced in 2014

with an innovative multi-material, multi-color automatic FDM system printing over 120

materials including 100 Digital materials. Transparent materials, rigid opaque materials

(different shades of colors), rubber-like materials (different shore values), simulated

polypropylene materials and high-temperature material.



**Figure 8**  Stratasys Objet Connex 3D printer

With soluble support materials like Fullcure 705 which is non-toxic gel-like

photopolymer support which can be removed very easily through pressurized water

cleaning system. Stratasys can have layer height of 16 microns which makes it ideal for

precision machining and rapid prototyping. Build size of the bed is $490 \times 390 \times 200$ mm.

The machine automatically calculates all the required parameters of the printing such as

layer height, UV light power, the feed rate of the photopolymer, the speed of the jetter

head along x and y-axis and displacement of the bed in the z-direction. Stratasys comes with the Objet Studio software which is used to place the model onto the build tray and validate its geometry, placement of sample and assigning the materials for the different parts of the model. Then it slices the model into a required number of layers and sends the information (G-code) to the printer where it starts printing. The samples are printed out with support material which is washed away and is ready to use.

## 3.3 Dynamic Impact Loading:

**Drop test machine:** After the fabrication of sample, next step is the dynamic loading of the sample. Drop tower used for the dynamic impact of the sample. It is a fully motorized tri-axial impact machine from CADEX. In

2 — Soft release system

1

3 — Time Gate (velocimeter)

Drop arm

5

Guide Rail

4 — Impactor to be mounted on the drop arm

Load cell

Drop Tower

Manual control
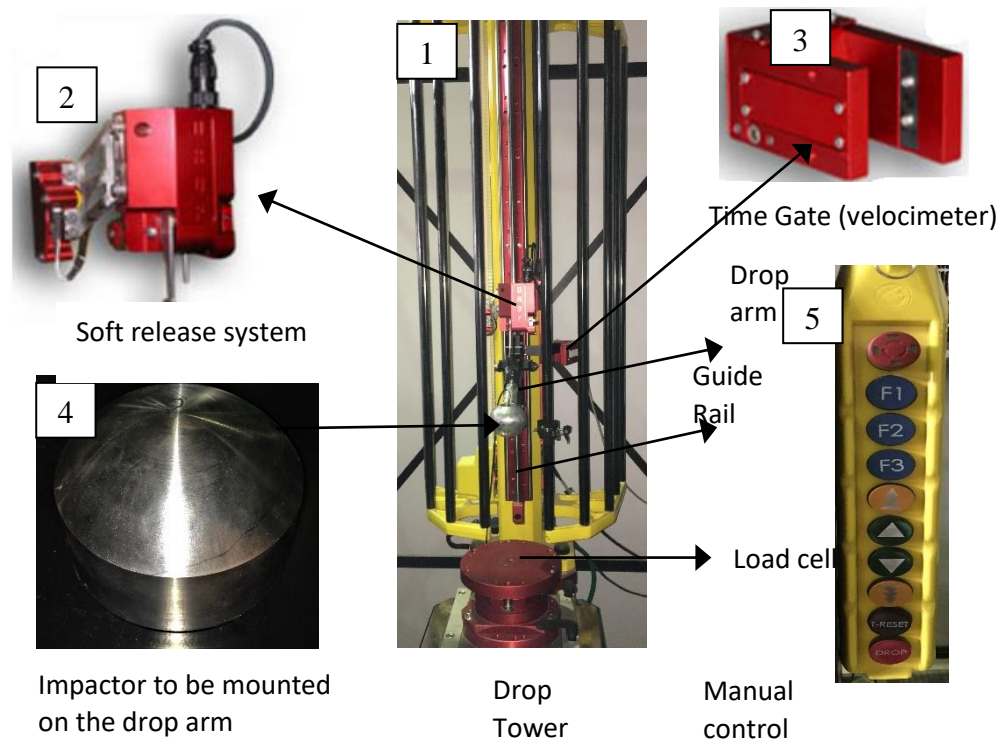
*Figure 9* all main parts of the machine are shown. In the drop tower test impactor is sent up to the required height along the guide rail and dropped onto the sample. The impactor is released by the soft release system in (2) which carries the drop arm up after the test is completed and locks in the position set. The soft release system is hydraulically controlled with an air pressure of 100 psi. Sub-image 4 shows the Stainless-steel impactor to be dropped on the sample to the height which weighs 4147 grams along with drop arm and clamp. Sub-image 5 depicts the manual control with preset test conditions of F1, F2, F3 and yellow, green buttons to move the drop arm along the guide rail with high and low values respectively.
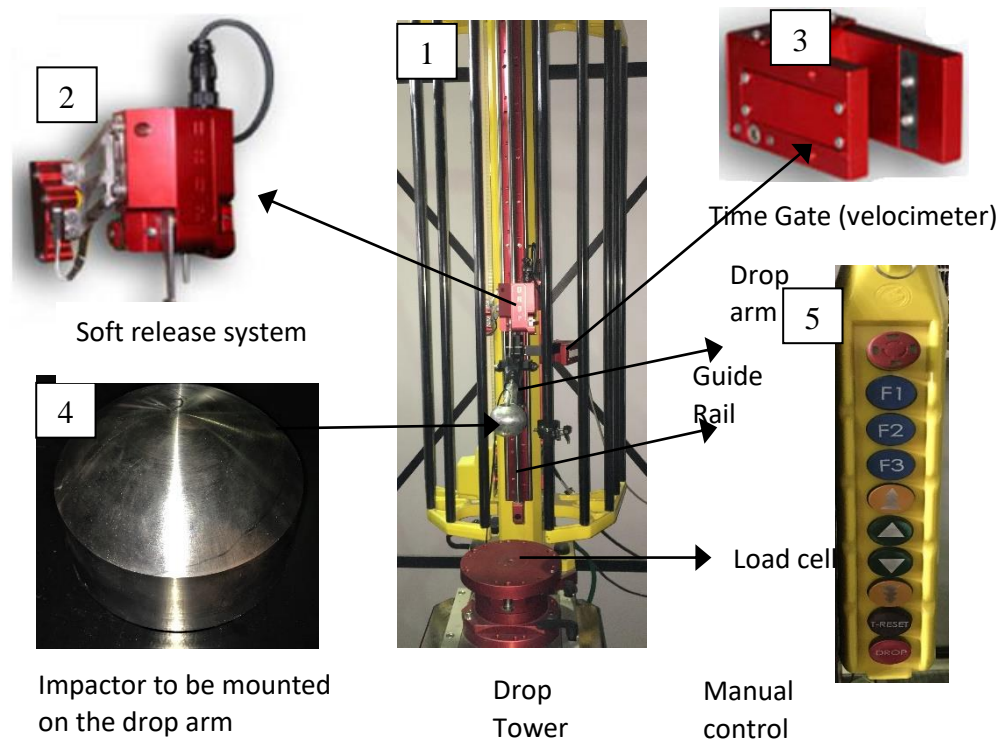
**Figure 9** Dynamic Impact test machine – Drop test tower

**Experimental input**: Sample dimensions are 10 cm x 10 cm x 5 cm, the thickness of the soft phase is 1 mm. consisting of 15 layers of bricks stacked vertically and 4 layers of bricks horizontally. The thickness of the brick is 24 mm x 56 mm. Height of the drop is 5 m.

**Fixed boundary condition**: In this case, the sample is fixed onto the load cell and the impactor is dropped onto the sample. The sample cracks and can be seen in Figure 10, we can see multiple cracks developed in the sample. Figure 10 shows different types of cracks in the sample of the brick-mortar structure fixed to the load cell.

The insets in the figure show initially the damage in the initial brick of contact from the impactor, next we have the cracks across the bricks for the 1-6 numbered bricks and a vertical crack on the bottom of the sample. Figure 11 depicts the enlarged images from previous figure insets. Bricks labeled 1-6 have cracks across the bricks, this may be due to the reflected waves from the corners of the samples. It is interesting to note that the cracks in bricks appear only at the top, bottom and near the center of the surface.
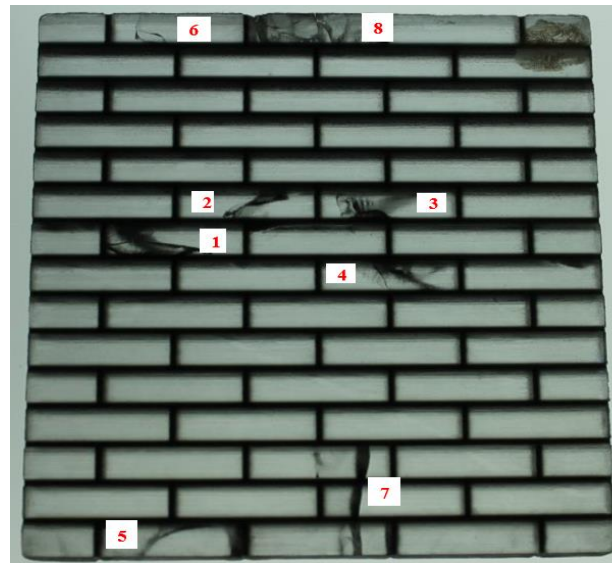


**Figure 10** Damaged sample with the fixed boundary condition (attached to the load cell) on left and the insets images enlarged below
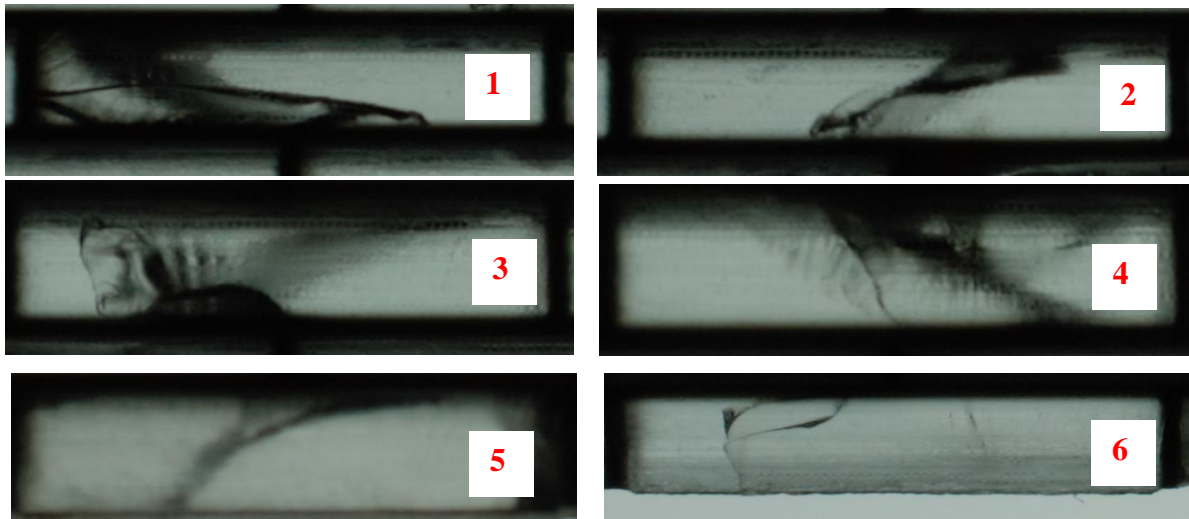
**Cracks crossing the brick structures**
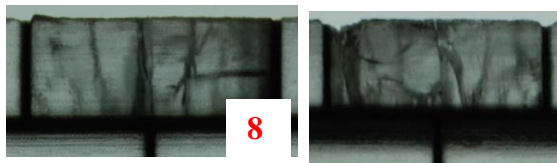


Damage on the top brick front (left) and back (right), shattered brick, multiple cracks through the brick
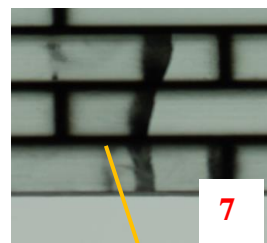
Vertical crack across the brick layers front (left) and back right)
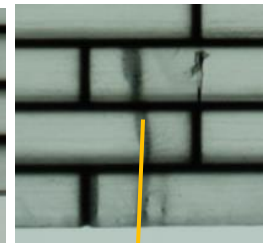
No vertical crack across the brick layers on the back

**Figure 11** Damages in individual brick insets from the previous image

The distribution of cracks hints at the controlled wave propagations to be studied computationally. The soft phase rubber around these bricks appears to be compressed, hence the deformation in the soft phase also has to be further investigated. This vertical crack is only on the front face of the sample and not on the back face of the sample. The impactor is large compared to the sample, the center of the sample is compressed from the top and may have caused tearing of the sample at the bottom end causing the vertical crack.

It is worth noting that the sample is printed on X-Y face building along the thickness of the sample. This makes sure the layers are in Z-direction and the adhesive properties between layers are available here. The vertical crack might have started at one surface and breaking the layers through the thickness but not completely through the surface.

These tests were not conclusive as the boundary conditions for this included a steel bed mounted on a load cell. To replicate this experiment in a simulation we must model the steel bed because the reflecting waves from the steel bed play an important role in the damage. Also, it is hard to determine the damage is only due to the normal impact force of the impactor and does not include any other effects like buckling. The computational cost to model the steel bed in peridynamics was beyond our computational power hence was inconclusive.

**Free body boundary condition test :** For understanding the impact wave patterns and studying the crack growth it is ideal to have an impact on the free body boundary conditions. Free body conditions were replicated by suspending the sample with thin thread attached with tape to the sample so that as soon as the impact takes place the sample easily falls onto the bed.

To stop the impactor from rebounding, a Styrofoam bed with a hollow cut is used, such that only the sample is fallen into the hollow portion and impactor is stopped by the styrofoam bed Figure 12.

In Figure 12, there is a clear description of the sample suspended and supported by Styrofoam bed which is approximately $11 \times 9 \times 9$ inches with a hollow cut through of $4 \times 3 \times 9$ inches for the sample to fall into after the impact. This hollow part is stuffed with soft feathers do that there is a minimum reflection from boundaries for the sample after impact. Hence the experiment consists of suspending the sample appropriately and loading the Drop tower with required conditions for the impact which requires setting up the number of impacts, height and time gate position. Velocity is recorded with the velocity meter (also known as time gate) which records the time just before impact is taking place.

Time gate as shown in

2 — Soft release system

1 — Drop Tower

3 — Time Gate (velocimeter)

Drop arm

Guide Rail

5 — Manual control

Load cell

4 — Impactor to be mounted on the drop arm
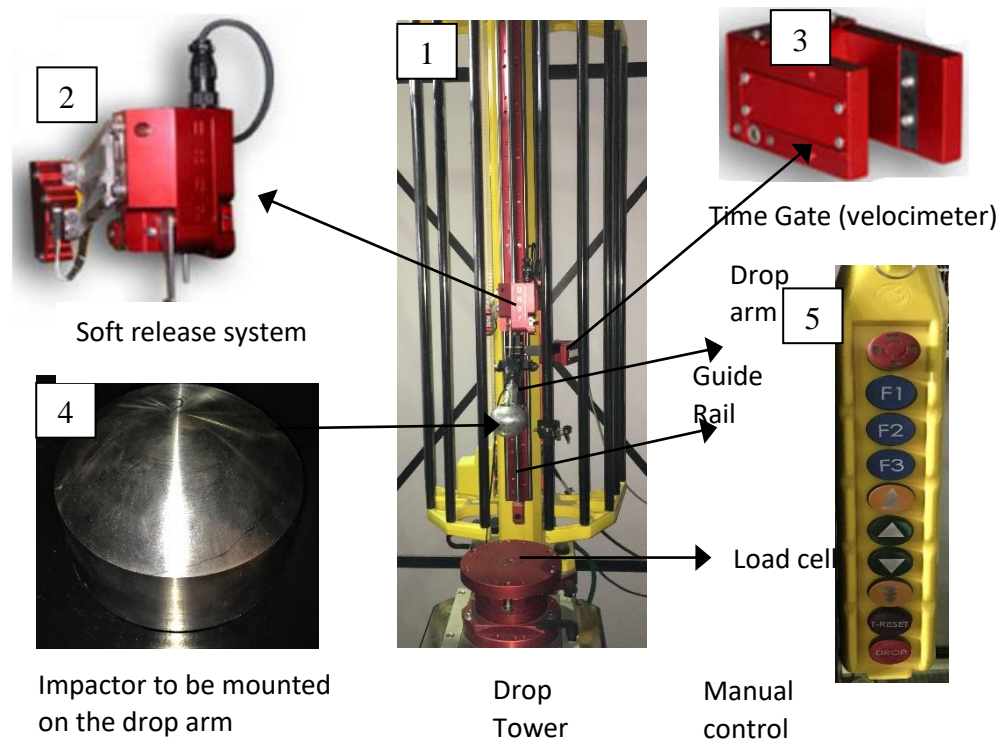
*Figure 9* sub-image 3 is placed at the height of suspended sample before the experiment. After setting all this drop button is pushed and the impact takes place. There is a mesh railing around the drop tower to prevent any accidents and safety eyewear is used to avoid accidental chips of sample flying after the impact test. After the test velocity and drop height are recorded.

## 3.4  Experiment Conclusions:

By the free body suspension, the samples were not damaged by the low-impact drop tower.  The sample was too strong to break and did not yield the required results. Next, the sample was impacted with a fixed boundary condition on a support, bed was impacted, and the sample damaged as seen in Figure 10. But this was not able to be

replicated in computations as the steel bed was large compared to the sample,

approximately 25 cm in diameter and height vs 5 cm × 5 cm × 0.5 cm sample
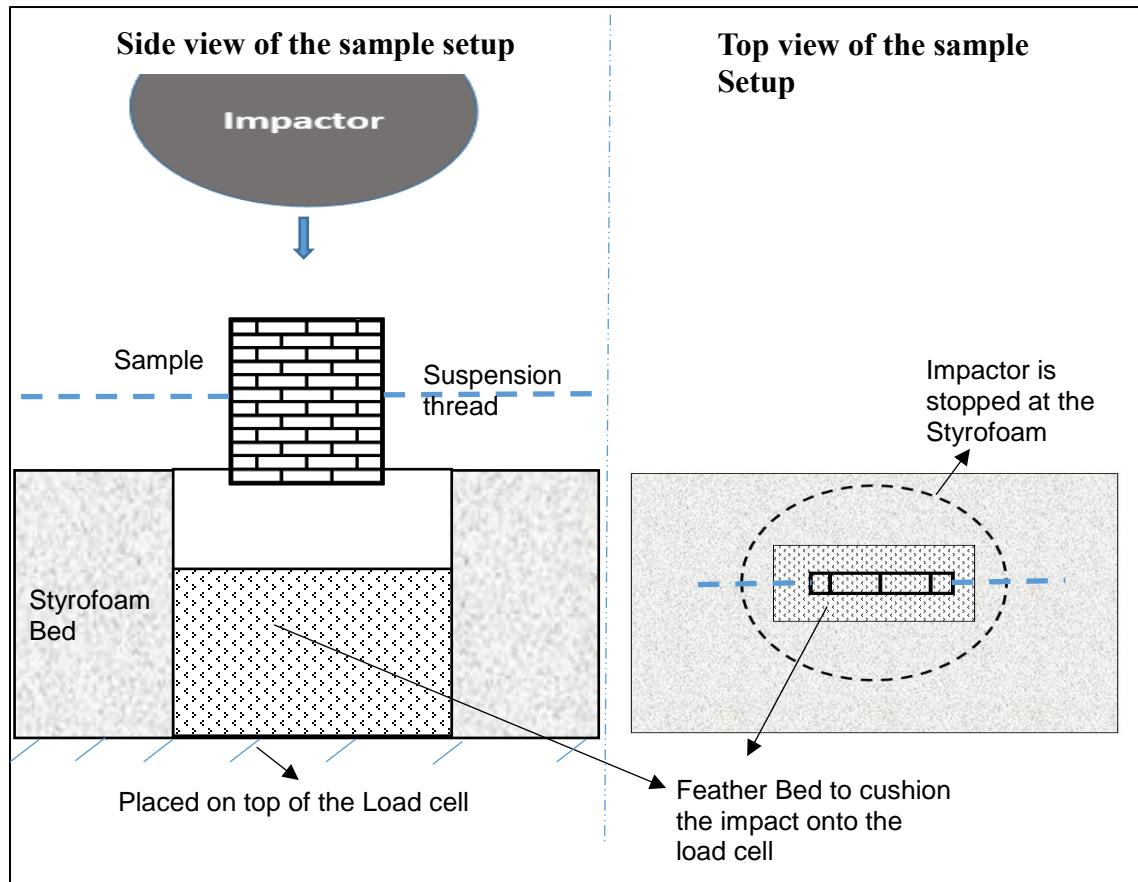


**Figure 12** Experimental setup for the approximate free body suspension of the sample

The number of nodes needed for a 3-tier brick-mortar model is around 1.9

million to capture the effect of soft phase effectively and is not possible to compute the

sample with fixed boundary conditions. To address this, we need to impact the sample

with a gas gun at velocities of 1000m/s. To capture the crack growth in the samples we

would have to use the high-speed camera with nanosecond shutter speeds. This complicated experiment procedure was not done due to time constraints and instead benchmark dynamic problem of Kalthoff-Winkler is used to validate against the 3D peridynamic model.

## CHAPTER 4: PERIDYNAMIC MODELLING

### 4.1 Peridynamic Modelling

Peridynamics is a non-local theory of mechanics which can perform both the classical continuum mechanics and molecular dynamics. Peridynamics extends the classical continuum mechanics to include discrete particles and growing cracks. In classical continuum mechanics, material points are influenced by the material points in its immediate vicinity. In the case of non-local mechanics, such as peridynamics, the material points are influenced by material points located in a certain region of influence or range defined as the horizon. Horizon ($\delta$), is the distance within which the material points have influence and can be easily visualized by a sphere in 3D case.

The PD (peridynamic) equations of motion at point $x$ at time $t$ for the bond based model are [33]

$$\rho_{(x)}\ddot{u}(x,t) = \int_{Hx} f(u(\hat{x},t) - u(x,t), x - \hat{x}) \, dV_x \quad + b(x,t)$$
$$\text{For } x \in \Omega \text{ and} t \in (t_0, \infty)$$

$$(4.1)$$

where $\Omega$ is the domain occupied by the body, $t_0$ is some initial tine, u is the displacement vector field, b is the body force vector and f is the pairwise force function in the

peridynamic bond that connects material points $x, \hat{x}$. The intergral is defined of over the region horizon,$Hx$. For microelastic material [33] a pairwise potential exists such that

$$f(\xi, \eta) = \frac{\partial \omega(\xi, \eta)}{\partial \eta} \qquad (4.2)$$

where $\xi = x - \hat{x}$ is the relative position and $\eta = u(\hat{x}, t) - u(x, t)$ is the relative displacement between points $\hat{x}$ and $x$. A linear micro elastic material is defined by micropoterntial $\omega$ as

$$\partial \omega(\eta, \xi) = \frac{c(\xi) s^2 \|\xi\|}{2} \qquad (4.3)$$

where $c(\xi)$ is the micromodulus function and s is the stretch in the PD bond.

$$s = \frac{\|\eta + \xi\| - \|\xi\|}{\|\xi\|} \qquad (4.4)$$

is the relative elongation of the bond connecting $\hat{x}$ and x. For a horizon region witch a spherical symmetry as in case of the 3D model, the corresponding pairwise function becomes

$$f(\xi, \eta) = \begin{cases} \dfrac{\eta + \xi}{\|\eta + \xi\|} C(\xi) s & \|\xi\| < \delta \\ 0, & \|\xi\| > \delta \end{cases} \qquad (4.5)$$

Assuming a specific form of the isotropic micromodulus function $c(\xi) = c(\|\xi\|)$, for example constant over the horizon region of varying linearly with $\|\xi\|$.The micromodulus function as defined in [34]. After discretization, material point, $x_{(k)}$ , is the center of a sphere (3D $horizon$), $\delta$, is the radius and the material points inside the sphere are the family of $x_{(k)}$ ,$Hx_{(k)}$.

For a damage dependent model the micro-potential is defined with a damage state ($\phi$) as $\omega(\eta, \xi, \phi)$. The damage state $\phi$ is a scalar quantity which cannot decrease over time, thus $0 \leq \phi \leq 1 \ \forall \ \xi \ \epsilon \ H$. And rate of damage growth is defined as $\dot{\phi} = \dot{D}(\xi, \eta)$ where D is deformation [35]. And for the materials where $\phi(\xi) = 1$ leads force field $f(\xi) = 0$ is termed as a material with a strong damage dependence.

All the material points within the horizon are connected by bonds or interactions, hence single material points are connected to all the material points in its horizon by means of interaction. The interaction of material points is defined through a micro-potential that depends on deformation and constitutive properties of the material.

In peridynamics, the motion of a body is analyzed by considering the interaction of a material point $x_{(k)}$, with the other, possibly infinitely many material points, $x_{(j)}$, with (j=1, 2,) in the body. The number of material points, the material point at the location $x_{(k)}$ inside the local region (horizon), $Hx_{(k)}$, shown in Figure 13 . Similarly, the material point $x_{(j)}$ interacts with material points in its own local region or family, $Hx_{(j)}$. Hence, when the horizon approaches zero the limiting case of PD becomes a classical theory of elasticity. Each material point $x_{(k)}$ with (k=1,2, 3,..) is associated with volume $V_{(k)}$, and a mass density of $\rho(x_{(k)})$. Each material point can be subjected to prescribed body loads, displacement, or velocity, resulting in motion and deformation.

With the cartesian coordinate system, a material point $x_{(k)}$ experiences a

displacement $u_{(k)}$, and its location is described by $y_{(k)}$ in the deformed state. The

displacement and body load vectors at material point $x_{(k)}$ are represented by

$u_{(k)}(x_{(k)}, t)$ $and$ $b_{(k)}(x_{(k)}, t)$ respectively. The stretch between material points $x_{(k)}$, and

$x_{(j)}$ is defined as

$$s_{(k)(j)} = \frac{\left( |y_{(j)} - y_{(k)}| - |x_{(j)} - x_{(k)}| \right)}{|x_{(j)} - x_{(k)}|} \qquad (4.6)$$

$$c = \frac{18k}{\pi \delta^4} \qquad (4.7)$$

where k is the bulk modulus, it can be expressed by Young's modulus of a material by

$E = 3k(1 - 2v)$ , where $v$ is the poison's ration (fixed ¼ for the 3D model) substituting

it in Equation (4.7) we have [36]

$$c = \frac{6E}{\pi(1 - 2v)\delta^4} = \frac{12E}{\pi \delta^4} \qquad (4.8)$$
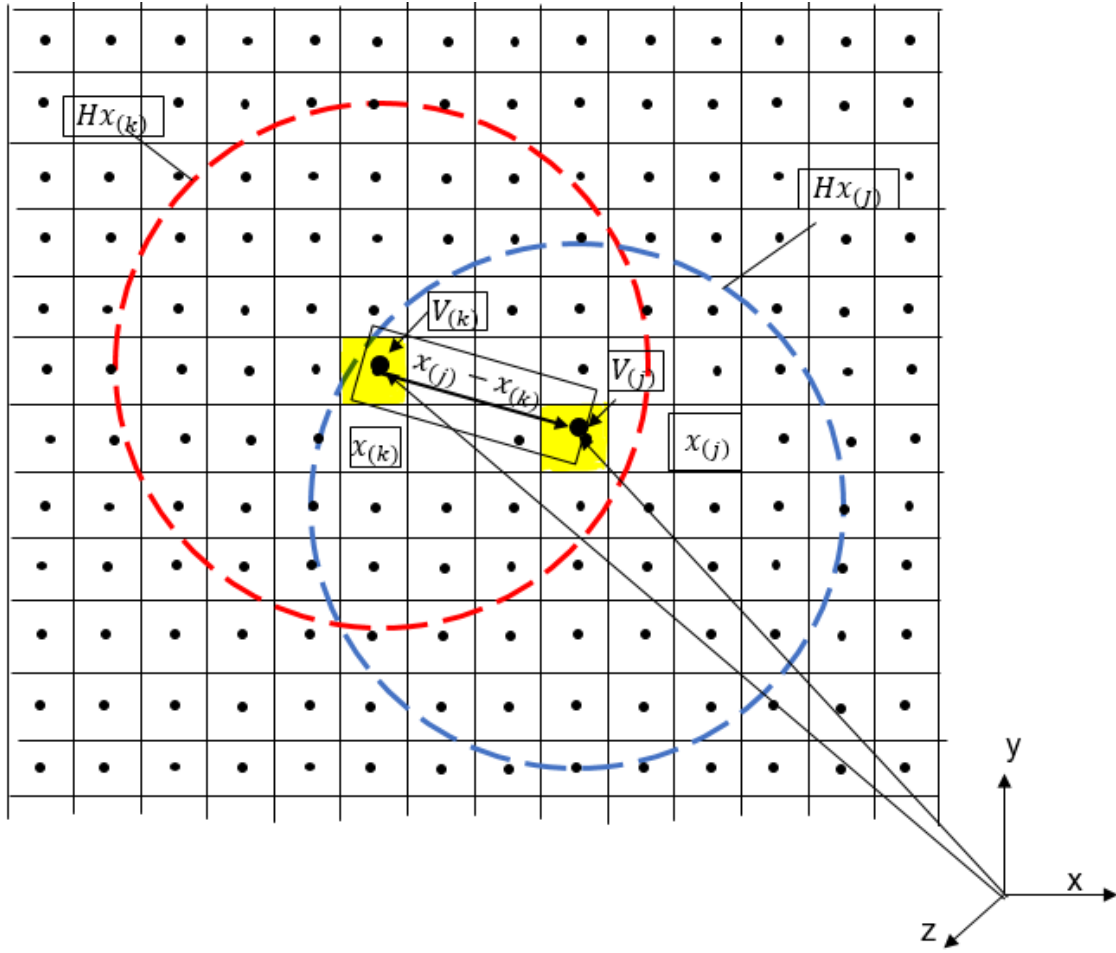
**Figure 13** Material PD points and interactions of points k and j located at $x_{(k)}$ and with horizons $Hx_{(k)}$ and $Hx_{(j)}$ with volumes indicated in a coordinate system. The relative distance between the points is at $x_{(j)}$- $x_{(k)}$. By which the deformations are calculated by relative positions of the material points $x_{(j)}$ , $x_{(k)}$.

To introduce damage,[34] introduced an irreversible bond breaking law as

$$f(\xi,\eta.x,t) = \begin{cases} f(\xi,\eta_1 x,\tilde{t}) < s_0 & for\ all\ 0 \leq \tilde{t} \leq t \\ 0 & otherwise \end{cases} \qquad (4.9)$$

The energy required per unit fracture area is found to be $G_0$ [34] derived from the following equation

$$G_0 = \frac{\pi c s^2 \delta^5}{10} \tag{4.8}$$

critical stretch $s_0$ is defined as the limiting value where the peridynamic bond breaks and is defined as

$$s_0 = \sqrt{\frac{10 G_0}{\pi c \delta^5}} = \sqrt{\frac{5 G_0}{9 k \delta}} \tag{4.11}$$

For the material points near the surface or at the boundary the number of nodes interacting is less than the material nodes completely inside the surface of the material. This implied the number of bonds a surface material point is almost half the number of bonds for the internal material points. As such the material points at the surface are weaker than the internal points as a number of bonds required to completely break are less and this constitutes a weaker material. To address this a surface correction method is used for the accurate representation of the material. There are several options in the literature for surface correction like introducing ghost or fictitious nodes outside of domain [37],[38] or compute approximate corrections for the micromoduli for the surface nodes in [39, 40]. We used volume method, in which uses stiffening factor to formulate bonds near boundary as

$$\lambda = \frac{2 V_0}{V_{(x)} - V_{(\hat{x})}} \tag{4.12}$$

where $\lambda$ is a dimensionless correction factor for the bond between the points $(x, \hat{x})$. $x, \hat{x}$ are two points near the boundary of the sample.

In 3D, $V_0 = \frac{4\pi\delta^3}{3}$; since $V_0$, is always greater then $V_{(x)}$ $and$ $V_{(\hat{x})}$ as latter are nesr the boundary and have less volume compared to the volume inside the material, $\lambda$ is greater than or equal to 1. The micromodulus of a bond then is

$$c_{corrected} = \lambda c$$

**Chapter 5: Kalthoff- Winkler Validation**

In this chapter, we will validate our peridynamic model by solving benchmark dynamic test, the Kalthoff-Winkler test. This chapter is organized in the following way first, the K-W experiment is described followed by a literature review of the K-W test. In the literature review, we discuss what methods were used to validate the K-W test in the past and their challenges and how peridynamic can overcome those challenges. Next, we discuss how the numerical model of our K-W is set up to match the experimental inputs and lastly, we see the results of the K-W test by our peridynamic model. We perform the K-W test for two discretization sizes and study the crack angle to validate the model.

**5.1  Kalthoff- Winkler Experiment**

Kalthoff-Winkler experiment is a dynamic fracture benchmark problem, it was conducted by Kalthoff and Winkler in 1988 [38]. The experiment consists of a steel plate with two notches (slits) as shown in Figure 14. The steel plate had no displacement constraints and was initially at rest. It is observed in the experiments that the impact leads to creating two cracks emerging from the notches and traveling to the outside boundaries of the samples as depicted in Figure 14, Impactor, also made of steel in the shape of a cylinder hits the steel plate's edge at a constant velocity of 32m/s. The damage captured by shadow photography [41].

In the experiments, the steel used is SAE 4340 with material properties listed below. The notches in the steel plate are tapered in the experiment, for simplicity we consider the notches to be rectangular with a width of 1.5mm. Geometrical parameters of the setup are in Figure 16 material properties are listed below:

| Material properties of steel for the set-up: | |
| --- | --- |
| Young's modulus | 191 GPa |
| Poisson's ratio | 0.25 |
| Density | 8000 kg/$m^3$ |
| Mass of impactor | 1.57 kg |

## 5.2  Literature Review of K-W tests:

In this literature review, we discuss different methods used to perform computational modeling of the K-W test, namely: finite element analysis, meshfree methods, and peridynamics. Their contributions and challenges for the dynamic crack propagation are discussed.

In [42], Needlemen and Tvergaard conducted one of the first FE analyses of the K-W experiment. The model was set up as a porous solid that accounts for ductile nature by the nucleation and growth of voids and they did not use the same material properties of the K-W experiment but a similar steel and modeled just the half of the plate due to symmetry. The initial velocity of the projectile was set to be zero and ramped to the velocity of 16.5m/s over a time of 1 μs. They assumed the notch width of 70 μm with a semicircular tip. In [43], the researchers used same parameters as Needlemen and Tvergaard with thermos-mechanically coupled finite simulations where the projectile face had applied velocity for 47 μs after which the surface is considered traction-free.

Contact forces were applied on either side of the notch to prevent interpenetration. In both cases researchers did not focus on crack propagation but instead on initiation of failure, stress and strain fields at notch tip hence did not report a crack angle but were used as a basis for future researchers for K-W tests.

In [44], to overcome discontinuity limitation of traditional finite element methods extended finite element (XFEM) method based on loss of hyperbolicity criterion was introduced. It extended FEM by enriching the solution space for solutions to differential equations with discontinuous functions for nodes which belonged to elements with discontinuities, such as fracture, by switching from continuum discontinuity to discrete discontinuity. A boundary condition of $u_y = 0$ was applied to the bottom face and a step velocity was applied to the face impacted by the projectile. The impact velocity was chosen as 16.5 m/s. The material properties of maraging steel type 18Ni1900 were used, with E = 190 GPa, Poisson's ratio = 0.3, and density = 8000 kg/$m^3$. The researchers obtained a nearly straight crack path originating from the notch tip at an angle of 58°, along with some damage found at the center not reported by K-W experiments. This was not a satisfactory comparison to the original experiment and needed further improvement.

Next, the cohesive zone elements were used with FE for observing crack propagation. In [45] Zhang and Paulino used intrinsic cohesive zone for K-W test, they used a fracture energy of 22.2 n/mm and cohesive strength of 1733 MPa. Several structured meshes composed of T6 elements of different sizes and aspect ratios were used and all simulations predicted crack path angle of 72 to 74 degrees, which were consistent to the experimental results.

They had to introduce a bilinear traction- separation law to minimize artificial compliance without making the solution unstable. Extrinsic cohesive zone method with adaptive mesh refinement and coarsening AMR &C [46], in this FE mesh, was altered during simulation and crack tip region was adaptively refined and areas away from crack were adaptively coarsened. The researchers obtained a crack angle of about 62° originating from the notch tip.

In [45], Nguyen used hybrid discontinuous Galerkin (DG)/ extrinsic cohesive zone method to simulate K-W problem. This hybrid method used DG to model pre-fracture behavior and extrinsic cohesive zone for post-fracture to eliminate the issue of artificial compliance. Nguyen obtained a crack angle of about 69° originating from the notch tip with an unstructured mesh of T3 elements. The results agreed well with the experiments, but the sharp transition from pre-fracture formulation to post-fracture formulation could potentially lead to instability in more complex problems all these results were heavily influenced by mesh. In [47], a combination of intrinsic and extrinsic cohesive elements hybrid was modeled to overcome challenges of both methods, but the crack depended entirely on the type of mesh and was not reliable for dynamic fracture studies.

Coming to meshfree methods, in [48], Raymond *et al*, smoothed particle hydrodynamics (SPH) method was used to conduct K-W test to study dynamic crack propagation in notched samples. In SPH, particles scattered across a domain and their interactions are defined by a kernel function that allows interpolating the quantities depending on the distance between the neighboring particles.

The SPH particle failure is defined by a critical stress and uses a cubic spline function to calculate outputs. For the test $\Delta$x=1mm is used, the cylindrical impactor is not rigid and the notch was introduced in the sample geometry of the model in shape conforming the notch. Angle propagation of 69.8 degrees. The reported simulated result was 1200 m/s, which is slightly larger than experimental observations. The SPH needs to be improved to match these changes.

In [49], To reduce the computational time of the meshfree methods , a scaled boundary finite element methods (SBFEM) with adaptive refinements with quadtree/octree meshes. The SBFEM was known for its success in unbounded domains and fracture applications but had displacement non-compatibility at the boundaries and this was overcome by remeshing the model at the crack tip with simple Boolean operations and octree mesh [49]. For the K-W test, they modeled just one half due to symmetry in the system. parameters used are as follows, Impact velocity 16.5m/s, material properties of 18Ni900 steel, Young's modulus E = 200 GPa, Poisson's ratio v = 0.3, density = 8000 kg/$m^3$ and static critical stress intensity factor $K_{IC}$= $68MPa.m^{0.5}$, $\Delta$t is 1 μs and angle observed is 77 degrees.

Computational efficiency of a peridynamic model is less than FEM, to address this Gu *et al*, [50] proposed a hybrid modeling of PD and FEM. The hybrid method dynamically switches from finite element computations to peridynamics based on a damage criterion defined on the peridynamics grid, which is coincident with the nodes of the finite element mesh, the crack angles are 64.2° and 69.6° for the single scale and multiscale cohesive elements simulations respectively.

They used 16.5 m/s for the 2D model. The peridynamic nodes are coincident with the finite element nodes, and nodal forces are computed either by finite element approximations (before PD bonds are broken) or peridynamics (after bonds are broken) based on damage criteria.

In 2017 [51], the Voronoi mesh was used for peridynamic modeling with dual horizon approach, ghost nodes and adaptive mesh refinement were also used to study the dynamic crack propagation. For 3D K-W test The Young modulus is $E$=191GPa, Poisson ratio is $\nu$=0.25, the mass density is $\rho$=8000kg/m3, and the critical stretch is $s_0$=0.01. The mass of the rigid cylinder projectile is $m$=1.57 kg, and the initial impact velocity is $v0$=32 m/s is used, The timestep =$8\times10-8$ seconds for 2000 steps. For the Voronoi-based PD simulations nonuniformly discretized with the 40,806 Voronoi material points were used. The ratio of horizon size and grid spacing, $m$, is 4, and report crack angles were in good agreement with that of the test. Although the proposed Voronoi-based PD can reproduce the progressive cracking reasonably, the dependence of the crack paths on the discretized grids was still an important problem needed to be addressed.

In [52] Silling used EMU code for the K-W computational test and reported an angle of 68° which is close to the angle of the K-W experiment, this would be ideal to achieve with our model. The impactor is assumed to be rigid and after the impact, the cracks grow from the notches to the outside boundary of the steel plate for this test. In [53] dual horizon peridynamics was used for the K-W tests.

Crack angles of 67.6° and 64.7° were reported in [54] with some additional imposed conditions like zero-failure for the top three layers of nodes is implemented, and the steel alloy used by them is different than the K-W experiment. In [54] a 2D uniform grid used for K-W test matched the crack angles with the experiment very closely at 68° but the initial velocity used for the impactor is 16.5m/s, which is smaller than the 32m/s used in the experiment.

To summarize the literature review, researchers in [42], were first to use FEA for the dynamic crack propagation analysis of K-W test, they analyzed stresses and strains near the notch and not the crack patterns due to discontinuities could not be modeled in FEA. In [44] to tackle the discontinuities extended FEM was used where the elements with discontinuities were solved by discrete methods and other elements were solved by traditional FEA formulations, but the crack angle was not matched effectively as the overlapping of both methods was not as expected. Next, cohesive zone elements of both intrinsic, extrinsic types and combination of both are used to model the cracks, but these models depended heavily on the mesh and were not reliable. Moving away from finite elements some meshfree methods were compared to K-W experiment such as SPH, SBFEM with better results than traditional finite element analysis. The computational cost is very high for these methods compared to the peridynamic model. Even though the peridynamics is computationally less costly than meshfree methods it is still not as effective as FEA. To overcome this, a hybrid of FEA and PD was used in 2017 [50]. Similarly, in [51] Voronoi mesh was used to mitigate the computational cost but the crack was highly dependent on the mesh and was hence not reliable.

In [52], used PD to model K-W test and was successful, in [55] dual horizon was proposed for better results, but still needs further studies. We used PD model described in the previous chapter to model our K-W test.

## 5.3    Numerical Model Set-up

For our K-W test, we used two discretization sizes of 1mm and 0.75 mm for the test. As discussed, the notch is a crucial part that determines the crack path initiation. We describe how we modeled the notch for our test in this section and list all the geometric, peridynamic parameters used for the test.

For our K-W test, we used Silling's test [52] as a reference point to start our tests, he used a discretization of 1 mm grid spacing and horizon of 3.15mm. In the model setup, one important aspect for Kalthoff-Winkler test is the creation of notch in the sample. In Peridynamics just removing the material nodes in the notch is not enough. Because if the notch size (1.5mm) is less than the horizon (m=3.105, dx=1mm) there will be bonds across the notch from one end to the other of the notch. This creates a weaker material instead of the notch required. For creating the notch in the sample, we give the boundaries of the notch region as inputs and identify the bonds within the boundaries of the notch and eliminate all the bonds in that region. For example, in our test the notch dimensions are 1.5mm $\times$ 50mm $\times$ 9mm, we specify these dimensions of the notch at their coordinates of ( -50,0) and (50,0) for left and right notches respectively.
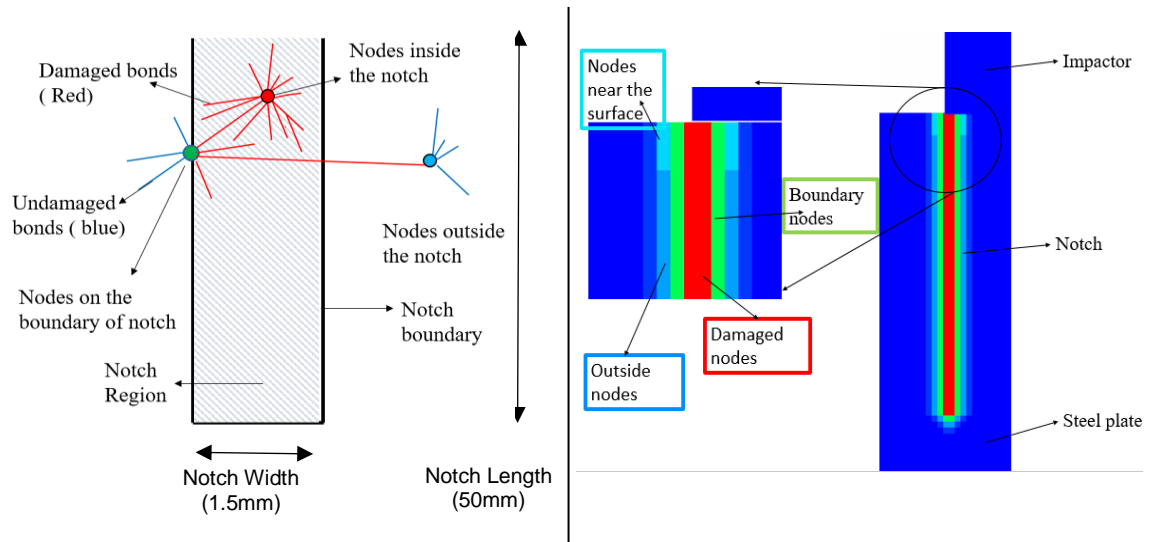
**Figure 14**  Notch creation in the model, depicting the damaged bonds and nodes in the notch region on the left and enhanced image of damaged nodes in the notch and its immediate surrounding region from the test on the right.

Figure 14, depicts the types of nodes and bonds in the notch. After defining the notch boundary, the notch region is established and all the bonds in that region are broken, broken bonds are depicted in red and undamaged bonds are depicted with blue. There are three types of nodes near the notch, nodes which fall completely inside the notch boundary, nodes which are at the boundary of the notch and nodes which are outside of the notch. For the nodes inside the notch all bonds are broken with the surrounding nodes, hence the damage is 100% and is depicted in red. For the nodes on the boundary of the notch bonds passing the notch region are broken and on the other side the bonds are not broken, and damage is estimated to be half and is represented with green and for the nodes outside the notch, some bonds crossing over are broken to create the notch and are depicted with a light blue color.
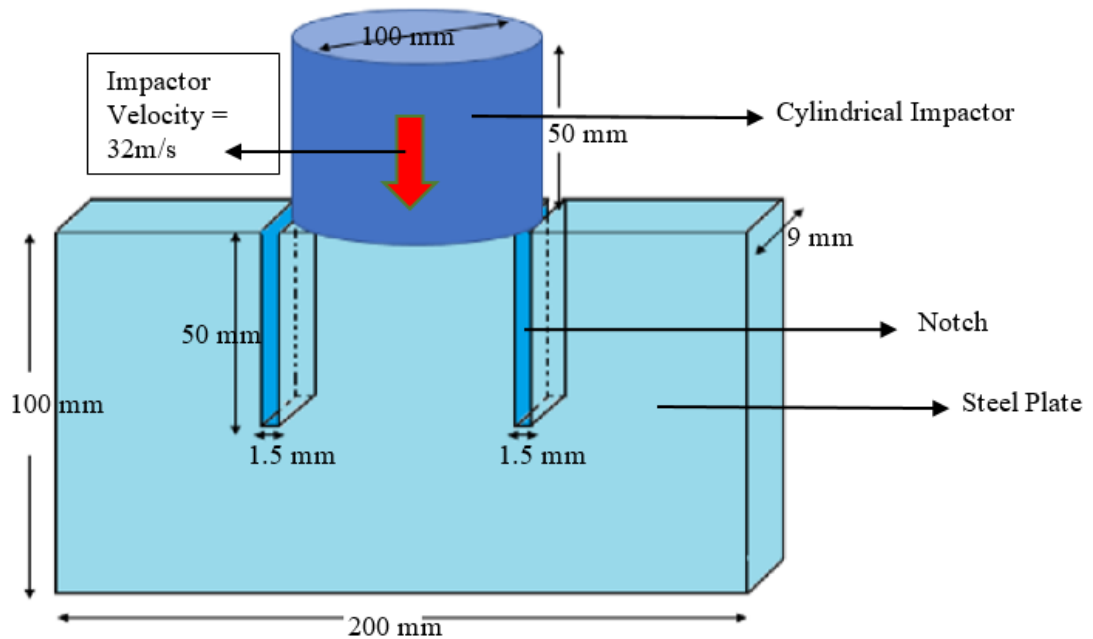
**Figure 15** Kalthoff - Winkler test setup and geometrical parameters
(the figure is not to scale).

Nodes near the surface have fewer bonds than the nodes inside the sample hence

there is a color variation indicating mode bonds are lost for the nodes near the surface due

to corners. Figure 15 shows the initial test conditions and setup of the K-W test. Surface

correction is carried out for the sample along the edges and cylindrical impactor is

modeled as rigid with no damage imposed on the nodes of the cylinder. Material

properties and peridynamic parameters such as discretization and horizon sizes used are

listed below. All the images show the planar view of the K-W test and it is a 3D model

with 9mm thickness. Peridynamic parameters used are listed in the table below

Input Parameters for the K-W test:

Peridynamic parameters

| | |
|---|---|
| Discretization size dx | 1mm |
| Horizon $\delta$ | 3.105 |
| Incremental volume of material points $\Delta V$ | $1 \times 10^{-9} m^3$ |
| Time step size $\Delta t$ | $0.01 \, \mu s$ |
| Total timesteps | 20,000 |
| Young's Modulus E | 191 GPa |
| Stress Intensity Factor $K_{IC}$ | $90 \, MPa.m^{0.5}$ |
| Fracture energy $G_0$ ( $G_0 = K_{IC}^2/E$) | $42.4 \, MPa.mm$ |
| Surface correction | ON |
| Short range forces | ON |

Applying above parameters the K-W test is done for 200 $\mu s$ for each test and data

is analyzed for the crack angle to match the experiments. The Impactor is placed at two

horizon distances above the surface. This is because in our PD model the bonds are

generated from the nodes which are in the family of the horizon, to prevent any bonds

generated between the sample and the impactor nodes we keep them apart. Then the

impactor is given an initial velocity with higher timesteps to reach the steel plate in 10

initial timesteps. The impactor is given the additional condition of zero-damage to model

it to be a theoretically rigid body.

**5.4     K-W test simulation results**

The K-W test simulations resulted in the crack propagation as expected and match the experimental results pattern as seen in Figure 16.
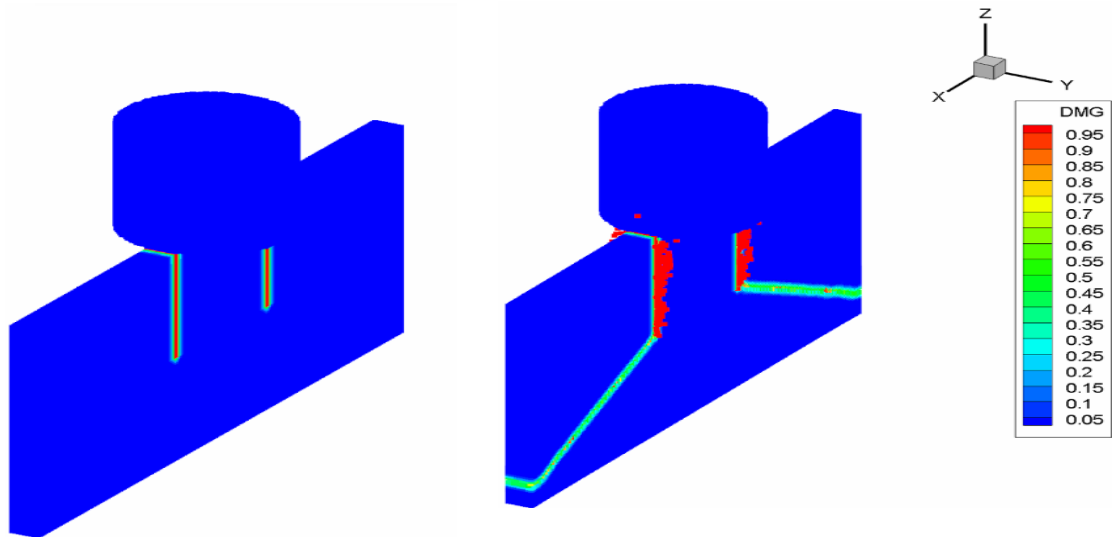


**Figure 16**  Initial time step of the K-W test on the lest and final timestep of the K-W test on the right

The scattered red nodes on the final step are from the notch. During the creation of the notch, the nodes broken left as is and the impact scatters them. We have discussed earlier in the numerical model that while creating the notch we cut the bonds of all the nodes in the region on at the end of the notch the nodes have the pre-damaged bonds up to two layers below the notch as seen in Figure 17 where green nodes represent bonds with 50% broken bonds and a light blue indicate nodes with some bonds broken. The impactor is positioned at the half of the notch and one layer of nodes in the notch are in direct contact with an impactor and they move freely during the impact scattering the remaining nodes in the notch.
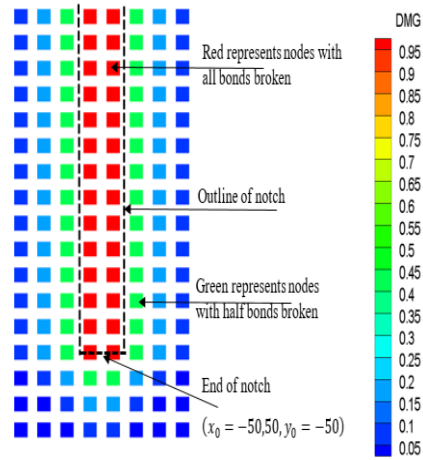
**Figure 17** Enhanced image of damaged nodes in the notch and its immediate surrounding region on the right.

Figure 18 depicts a processed image of the final simulation step for dx=1mm, in planar view, where the nodes with damage greater the 90% are removed for the better visualization of the crack as it hides the scattered nodes in the notch. The scattering ratio of the plot is set to 50% for a better understanding of the crack initiation. From Figure 18 we can clearly see the crack initiates at the corners of each notch. This is expected as the corner of the notch is a stress zone, the crack angles are calculated for the corner tip for the simulations. The angle between the vertical plane of the impactor and the crack at the corner of the notch from where the crack initiated was measured by Autocad. We drew two lines, one coinciding the vertical plane of the impactor/ notch and other coinciding the crack path from the corner of the notch where it started.
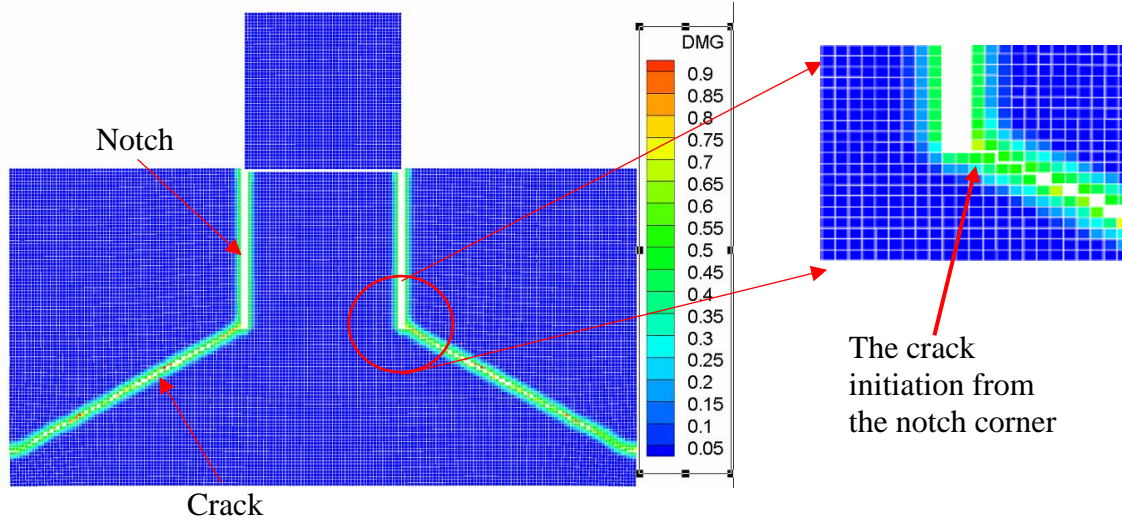
**Figure 18** Front- view of final timestep of the K-W test, with the post-processing of notch area and nodes downsized to half the original size. The magnified image on the right shows the crack initiates from the right corner from the right notch and similarly left corner from the left notch.
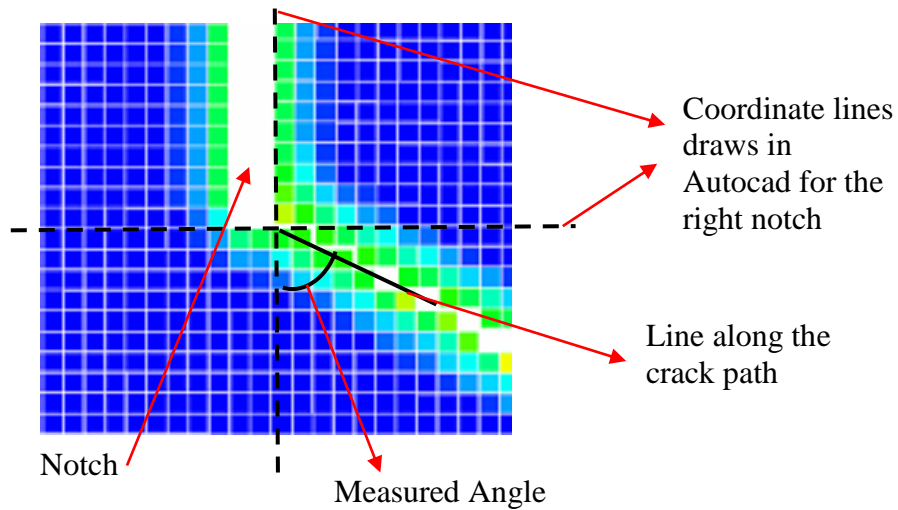


**Figure 19** Measurement of the crack angle by AutoCAD.

The crack started at approximately 800 nanoseconds for each case of discretization. Multiple measurements of the angles were taken at different time steps to see how the crack path changed. We observed that crack angle with respect to the vertical plane started at a high angle and then decreased slightly finally flattening out at the end to be nearly horizontal to the surface. Different angles recorded for the left and right crack paths. For dx=1mm. The angles measured were $62° \pm 1°$ for the left crack and remained almost constant throughout the path and then flattened out at the end. For the right crack, however, the angle measured was $66°$ at 800 ns which changed to $63°$ at 1200ns and to $62° \, at \, 1600 \, ns$. The total time of the simulation was 2000 ns at which the crack flattened out. To further investigate this model, we simulated the Kalthoff- Winkler for a smaller discretization of dx=0.75 mm with the nodes 661,581. For this, the angles measured were $67° \pm 0.5°$ for the left crack and $69° \pm 0.5°$ fro the right crack which match with the experimental results closely.

This shows the convergence of the test from dx=1mm of the previous case where the initial crack angles measured were less, ($62°$, $66°$ for the left, right cracks), compared to the experimental values and for the finer discretization of dx=0.75mm

the initial crack angles measured were, ($67°$, $69°$) a lot closer to the experimental values reported. This validates our PD model for the dynamic crack propagation.
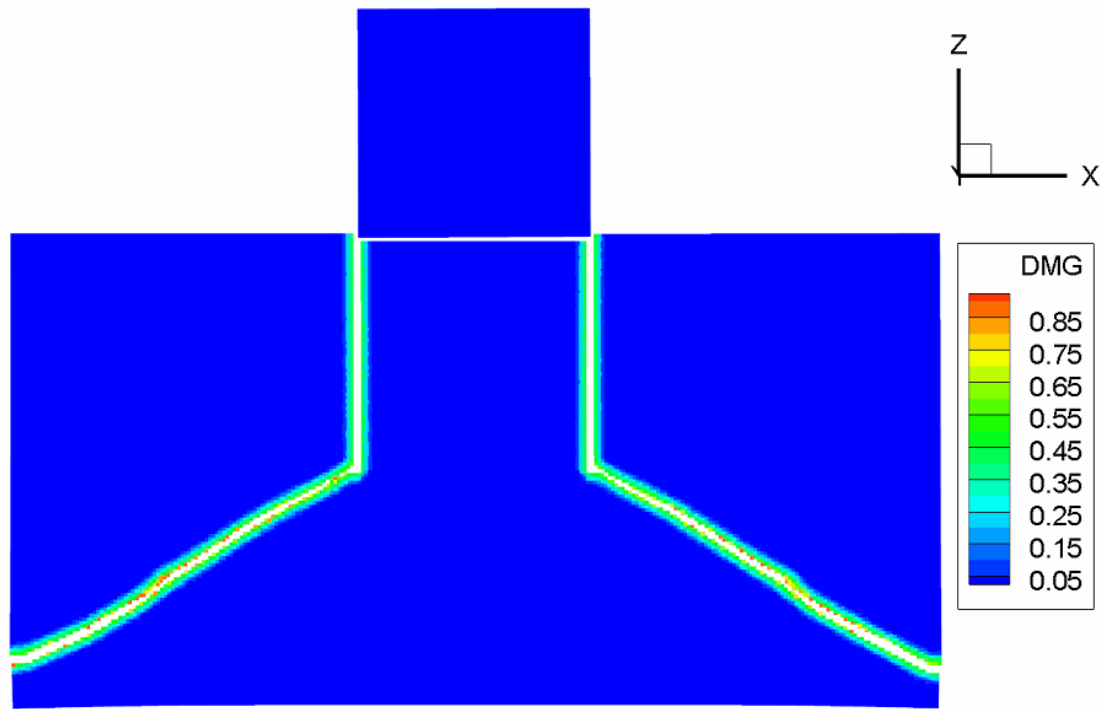
**Figure 20** Damage pattern for dx=0.75 mm. The crack pattern is clearly depicted in this case compared to the previous discretization. The color bar depicts the damage value and the image is post-processed for damage from 0 to 0.9.

Delta convergence study would be a good way to look at the convergence of the results. For this, at least three results would be ideal to compare. To do this if we go for a larger discretization greater than 1mm the size of the notch would be too big compared to the experiment. Because if we delete even one row of nodes for discretization say 1.5mm the notch would be 3 mm and cannot be used to test and finer discretization for dx=0.5mm must be implemented but is beyond our current computational ability and is the future work for this model.

# CHAPTER 6: MULTI-MATERIAL MODEL

In this chapter, we introduce the multi-material model containing stiff material and a soft material. First, we do a convergence study for the multi-material model with the brief introduction of the type of convergence studies in peridynamics. We observe the convergence in both m and $\delta$ convergence for our model. Then we introduce the bio-inspired structures gradually with different patterns starting from one horizontal layer, two horizontal layers, two tier brick-mortar structure and three tier brick-mortar structure. We then introduce a non-linear model for the soft phase for realistic damage in the model.

## 6.1    Convergence studies – delta convergence and m convergence

In peridynamics, there are three types of convergence tests namely m-convergence, $\delta$ convergence and $\delta$-m convergence [56, 57]. For our study, we do $\delta$ convergence and m-convergence. In $\delta$-convergence, $\delta \rightarrow 0$ and m $(= \delta/\Delta x)$ is fixed or increases with decreasing $\delta$ but at a slower rate. In this case, the numerical peridynamic approximation converges to an approximation of classical solution if it exists. The larger the m is, the closer the approximation becomes. The m-convergence: $\delta$ is fixed and m $\rightarrow$ $\infty$. The numerical peridynamic approximation converges to the exact nonlocal peridynamic solution for the given $\delta$. The number of material points every node increases and the solution converges as the $\Delta x$ becomes smaller and smaller.
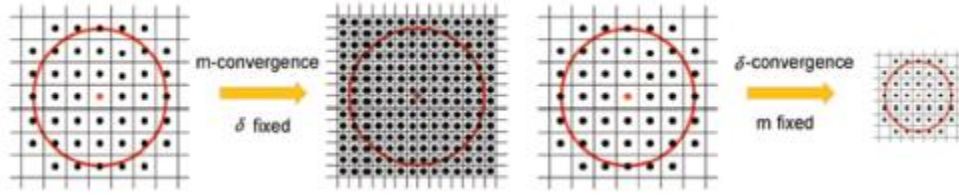
**Figure 21** Graphical representation of m-convergence on the left and delta convergence on the right [57]

For both convergence studies, we used a sample with a rectangular shape as Kalthoff-Winkler model with different dimensions. 50 mm × 25 mm × 5 mm. Instead of a cylindrical impactor, we used a spherical impactor to resonate with the test simulations of brick-mortar structures. In the previous section, we verified the model for dynamic loading now for the verification with two material models with the dynamic load we use the model with one horizontal layer of soft phase included in the sample at the center Figure 22. There are three types of bonds for the model, type 1 consists of bonds between stiff phase and stiff phase, type 2 consists of bonds between soft phase and soft phase, type 3 consists of bonds between stiff and soft phase, termed as an intermediate phase. The stiff phase represents approximate properties of PMMA and soft phase represents that of natural rubber. Linear elasticity is used for rubber material for simplicity. The impactor is of the stiff material to reduce the type of bonds in the peridynamic model. For all the tests the following parameters were used for the stiff, soft and intermediate phases:

Soft Phase:

Young's modulus = 2 MPa

Fracture energy $G_0$ =$1.04 \times 10^3 J / m^2$

density = 1015 kg/$m^3$

Stiff Phase:

Young's modulus = 3100 MPa

Fracture energy $G_0$ =$1.0 \times 10^{20} J / m^2$

Density = 1015 kg/$m^3$

Intermediate Phase:

Young's modulus = 100 MPa

Fracture energy $G_0$ =$1.0 \times 10^{20} J / m^2$

Density = 1015 kg/$m^3$
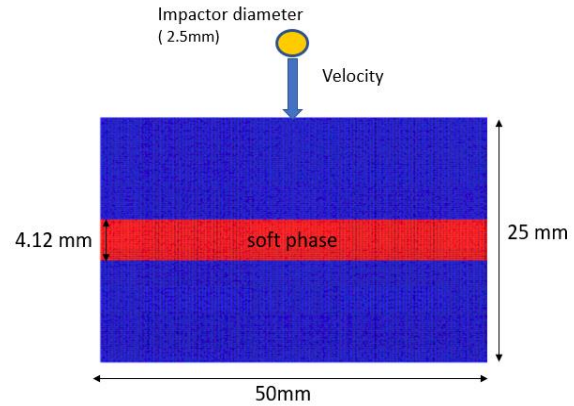


Figure 22 Test model for the convergence studies, one horizontal layer of the soft phase. Blue represents the stiff phase and red represents the soft phase. Impactor is spherical with 2.5mm diameter.

**M convergence**

M-convergence tests are done for the fixed $\delta$ of 2.08 mm, and uniform step size of 10 ns which is stable for all the test cases used. The impactor has a high initial velocity of 500 m/s, which was found to be ideal for the sample. As discussed earlier the impactor was aimed to have minimum contact time to analyze the damage and waves effectively.
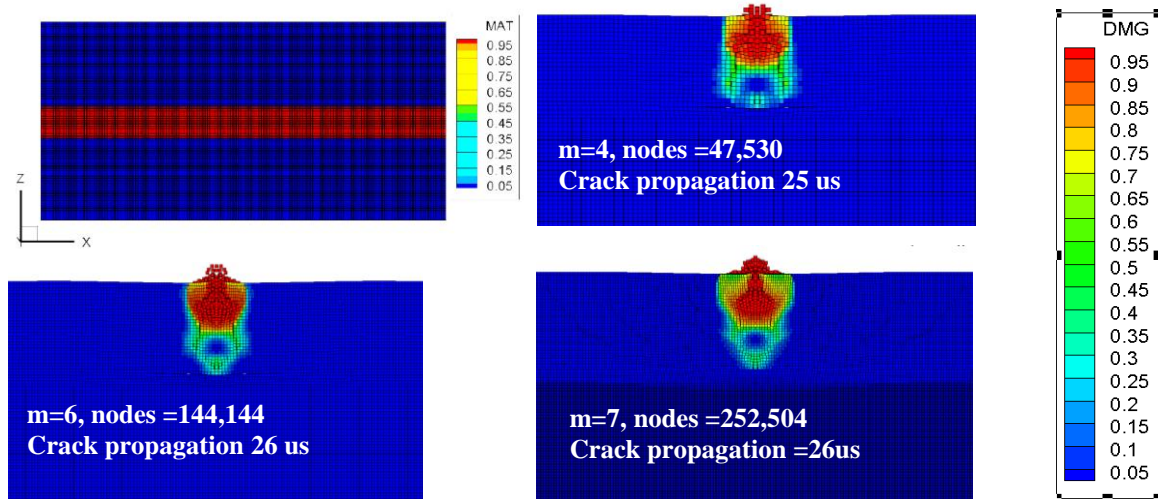
**Figure 23** m-convergence test

Lower the impactor and sample contact time is lower the impact waves are in the sample to be studied. So, we chose a velocity where the impactor hit the sample and bounced back instead of penetrating the sample or being embedded into the sample

First, we perform the *m*-convergence study for the with $\Delta x = 0.52$ mm for m= 4 (#nodes is 47,530), $\Delta x$= 0.35 mm for m = 6 (#nodes = 144,414) and $\Delta x$= 0.3 mm for m =7 (#nodes = 252504). In Figure 23, the upper left image represents the horizontal layer model used for the test and various m test results for the damage. The damage is indicated by the color legend on the right and indicates the percentage other f bonds breaking for a single material node. If all the bonds of the material are broken the damage is represented as red and if no bonds are broken it is represented with blue. We can see that at time 25 micro seconds the crack path is same for all the cases of m (=4,6,7). In m convergence test as the m increases the crack resolution is expected to increase due to the increased number of nodes in the horizon, that holds true for our case.

For *m*-convergence test, the *m* value is varied on a large scale, for example, m=2,4,8 *etc*., but for the 3D model, the smallest m to be used is 4, [57] and the computation cost limited the case up to m=7, hence the range of m=4,6,7 is used. Even though the crack pattern is coarse for m=4, it represents the damage accurately in terms of damage and crack path. Hence this value is chosen for the remaining brick mortar structures to be examined as well.

### *δ*-Convergence

For *δ* convergence test, m= 4 is fixed, and three different grid sizes are used. Coarsest model is *δ*= 2.8. With grid size of 0.7 mm (20,736 nodes), the next model has *δ*=2.08 with a grid size of 0.52 mm (47,530and nodes) and last being *δ*=1.4 mm with a grid size of 0.35 mm (144,144 nodes). In Figure 24, we can see different cases damage profiles. AS the horizon decreases the damage becomes concentrated at the crack tip, indicated the *δ* convergence for the model.
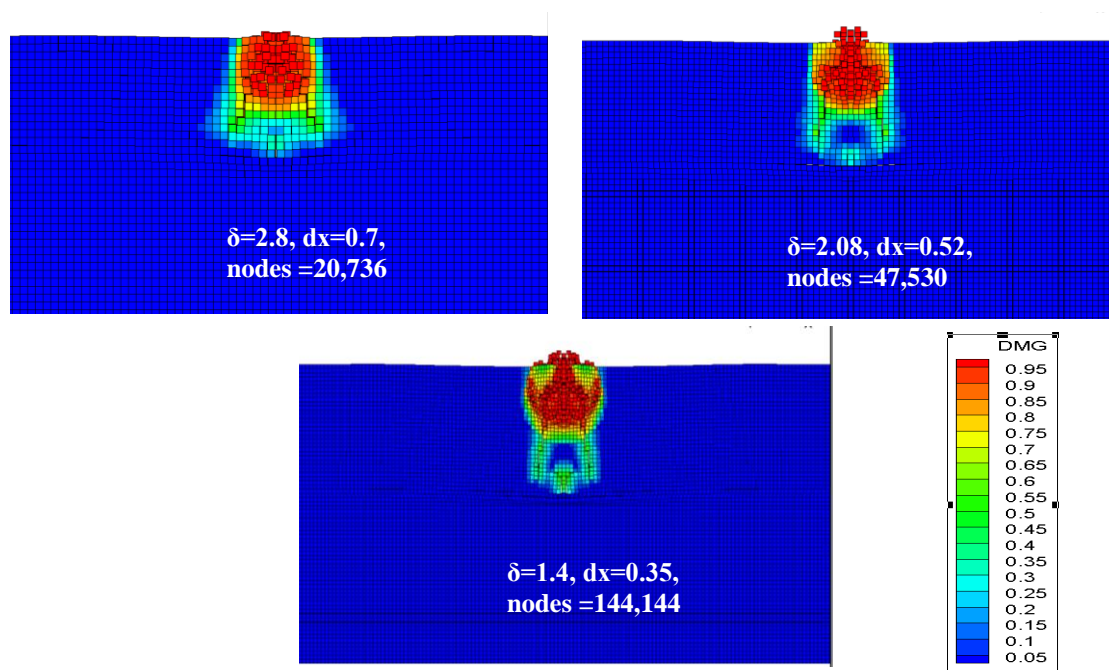
**Figure 24** Delta convergence

## 6.2    Bio-Inspired Patterns- Multi material Model

In the previous section, we have verified our peridynamic model by delta and m convergence tests. Validation of sample is done by Kalthoff- Winkler test. Now in this chapter, we test the damage in different brick-mortar samples with different patterns of soft phase in the sample. To accommodate the computational cost, we selected 20% volume ratio of soft phase to the original volume of phase. We still used the same stiff material spherical impactor with PMMA material and initial velocity to make it rebound from the surface of the sample.

The dimensions of the sample are 50 mm $\times$ 50 mm with 9 mm thickness in a direction perpendicular to the plane of impact. For the model to capture the displacement in the soft phase minimum number of nodes needed is 8. The horizon $\delta$ needs to be smaller than the thickness of the soft phase in the sample so that the horizon covers the soft phase and does not involve the intermediate phase consisting of bonds from both phases.  Keeping this in mind our first test sample consists of one horizontal layer of soft phase, next we have two horizontal layers of soft phases with same volume ratio of 20%, next we have our first brick-mortar structure consisting of 2 brick (stiff) and mortar (soft) phases, continuing till we have 3 layers of Bricks and Mortar with 20% volume ratio.

We impact all the samples with the impactor with an initial velocity of 500m/s and use a uniform timestep of size 10 nanoseconds which is stable for all test conditions. For the impactor to be at least the thickness of the sample we chose the diameter of the impactor to be 9mm. We change horizon ($\delta$) and grid spacing ($\Delta x$) for each case to

accommodate the soft phase for the sample. We use surface correction on and short-range

forces on all the samples. Following are the results of the simulations.
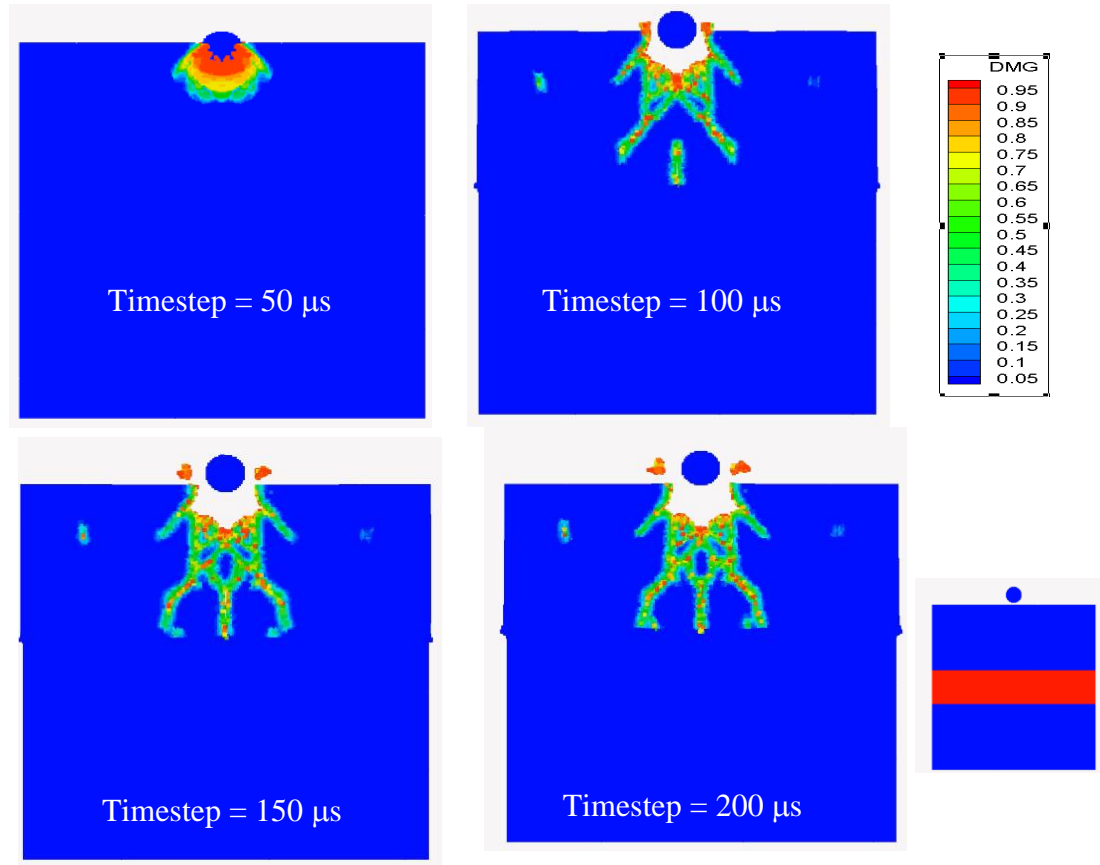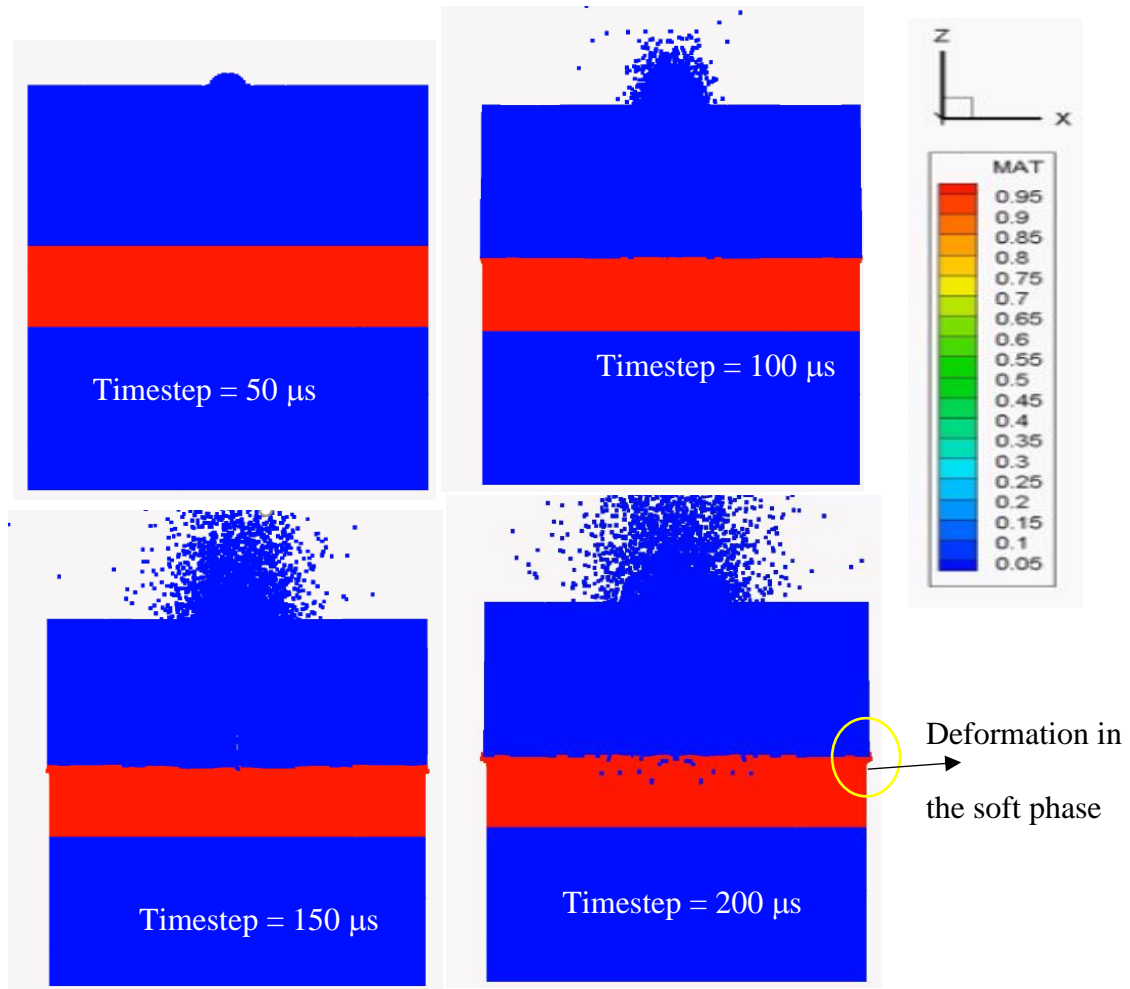


**Figure 25** Damage profile screenshots of one horizontal layer sample with the color bar
and axis on the right with the mini material distribution of the sample.

**One horizontal layer:**

For the horizontal layer, we can see initially the material distribution and impactor

is situated at the top of the sample with a uniform velocity of 500m/s. the total duration of

the sample is 200 μs, with a time step of 0.1 μs. Grid spacing $\Delta x$ is 0.5 mm, $\delta$ is 2 mm with m=4, a total number of nodes of 723,111 and soft phase is 40 nodes thick.

In Figure 25, we can see the damage profile of one horizontal layer soft phase structure progressing. Initially, the impactor hits the sample at 50 μs where the impactor's top portion can be seen and it is leaving the sample at 100μs, where impactor profile is more outside than in 50 μs. In the damage profile for better visualization completely nodes with damage more than 95% are removed. We can see the cracks emerging from the impact at 100 μs and progressing through 200 μs even after the impactor is leaving the sample. The damage stops after it reaches the soft phase and does not proceed to the second layer. We can see the impactor entering the sample and the material shattering around it.

**Figure 26**  Screenshots of material distribution in single horizontal layers

**Two horizontal layers:**



**Figure 27** Screenshots of damage profile in two horizontal layer samples
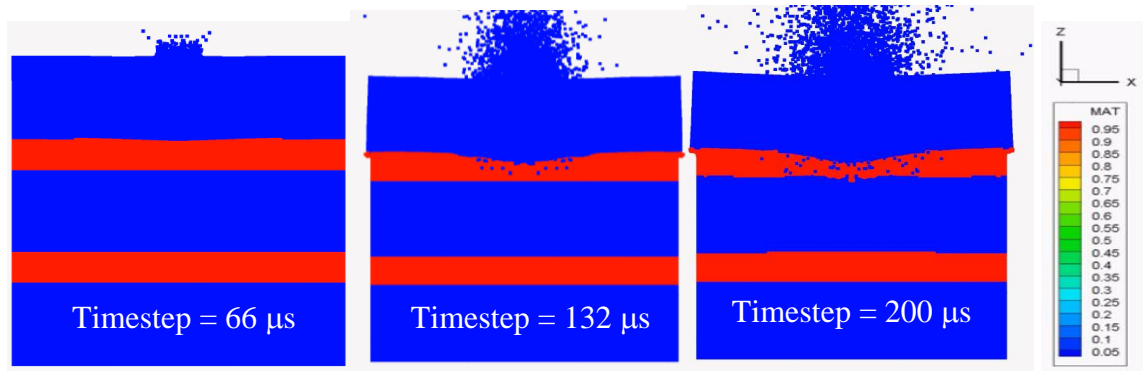


**Figure 28** Screenshots of material distribution in two horizontal layers
at different timesteps

In  Figure 25 and Figure 27 we can see the damage profile and material

distribution of the two-horizontal layer sample. Grid spacing $\Delta x$ is 0.5 mm,$\delta$ is 2 mm

with m=4, total number of nodes is 723,111 and soft phase is 20 nodes which is sufficient

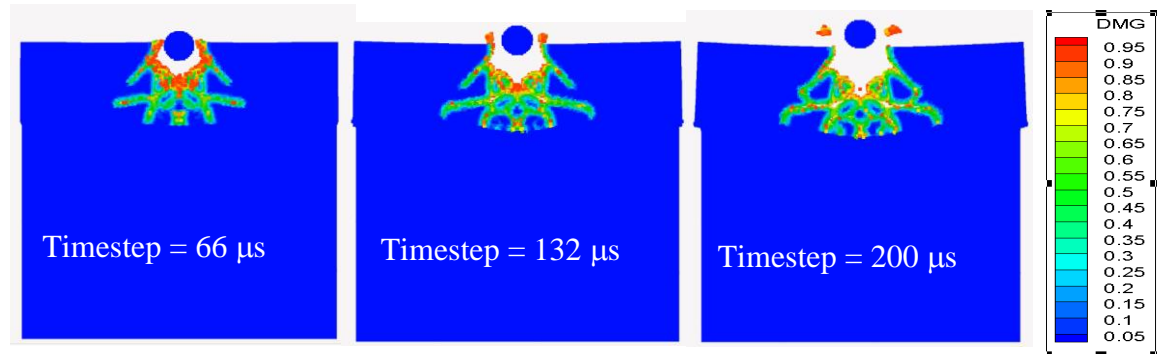to see the deformation in soft phase. Damage profile shows the cracks growing from the

impact at 66 μs and stopping at the horizontal layer, the cracks begin to grow even after

the impactor rebounds at 50 μs. in the material distribution, we can see the first layer of

soft phase being compressed and the second layer of soft having slight deformations. The cracks stop at the soft phase and do not damage the stiff phase under the soft layer. So, in both cases, the damage is constricted to the initial soft phase of the sample. Next, we see how the simple brick-mortar layer of two layers effect the damage in the sample.

**Two brick-mortar layer sample**

In the two-layer brick-mortar structure, the number of nodes is 732,975. Grid spacing $\Delta x$ is 0.5 mm, $\delta$ is 2 mm with m=4, and the nodes in soft phase is 14. In this, we can see the damage is again restricted to the soft phase and deformations in the soft phase can be clearly seen in Figure 28. Damage is again constricted to the first stiff brick of the sample.
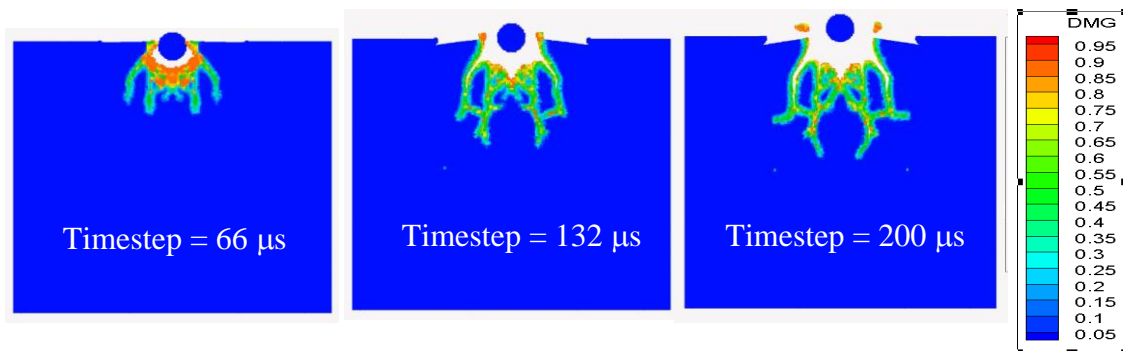


Figure 29  Screenshots of damage in the 2 brick-mortar layer structure
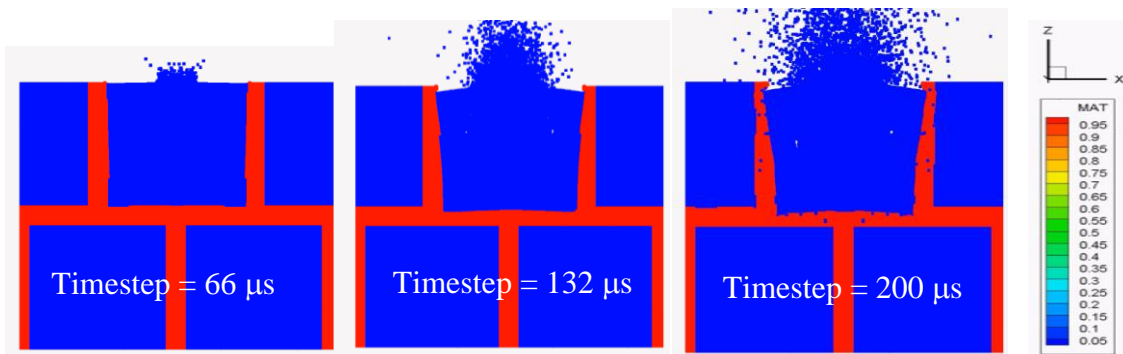


Figure 30  Screenshots of the material distribution of two brick-mortar layer structure

**Three brick-mortar layer structure:**
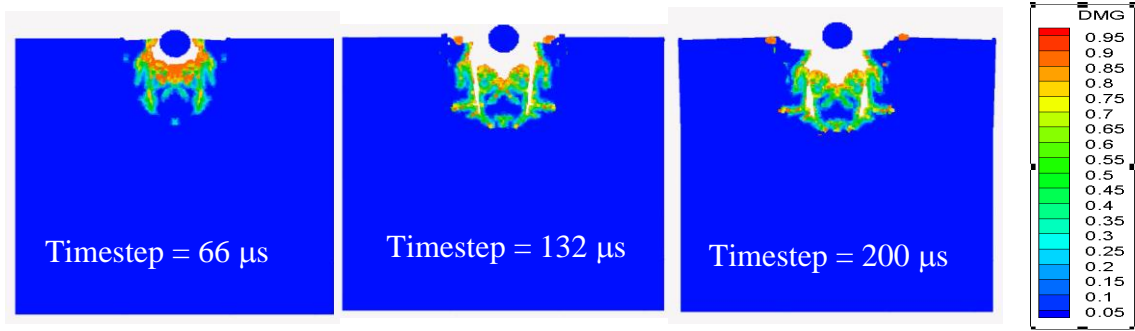


Figure 31  Screenshots of damage profile in 3 brick-mortar layer of structure
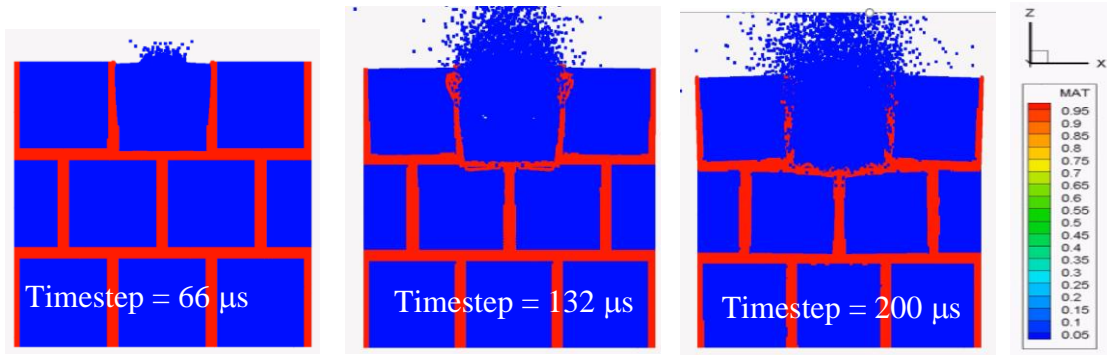


Figure 32  Screenshots of material distribution in 3 brick-mortar layer structure

In the three-layer brick-mortar structure the number of nodes is 722,823, grid spacing $\Delta x$ is 0.5 mm, $\delta$ is 2 mm with m=4, and the nodes in soft phase is 8. Like previous cases, the damage is restricted to the first stiff brick of the sample and the soft phase protects the remaining sample from damage.

## 6.3    Non-Linear Model for the Soft Phase

The material deformations in the soft phase are very drastic in this structure as seen in timestep 132µs in Figure 32. The soft phase deformation is not gradual and

appears as if the soft phase is split and there is a layer of hard phase in between. This is

clearly observed in the material distribution of soft phase only in the three-tier brick-

mortar structure in Figure 33. The initial brick has damage and soft phase surrounding the

brick is deformed to restrict the damage, the third layer is not damaged. The unrealistic

deformation is due to the linear stress-strain relationship used to model the rubber

material, which in reality has a non-linear elastic behavior. In figure 34 the non-linear

stress-strain is modeled and shows a realistic distribution of the soft phase. Damage

profiles can be seen in Figure 35 and it is same for both linear and non-linear elastic

models. Hence the damage predictions for the previous cases is correct. The unrealistic

damage is also may be caused by the lesser number of nodes in soft-phase for the three-

tire brick-mortar model which is not the case for previous models. The non-linear model

is defined by a piecewise continuous function. The natural rubber properties are

considered for the different elongation percentages and divided into 5 piecewise

functions as follows and shown in Figure 33

$$E_{(s)} = \begin{cases} 1.1184 & s \leq 1 \\ 0.5512 & 1 \leq s \leq 3 \\ 0.1089 & 3 \leq s \leq 4 \\ 1.8723 & 4 \leq s \leq 5 \\ 3.9667 & 5 \leq s \leq 6 \\ 6.3920 & s \geq 7 \end{cases}$$

Where E is Young's modulus in MPa, s is the strain % of the rubber, where 1 is 100% elongation and 7 is

700% elongation *etc*.[58]
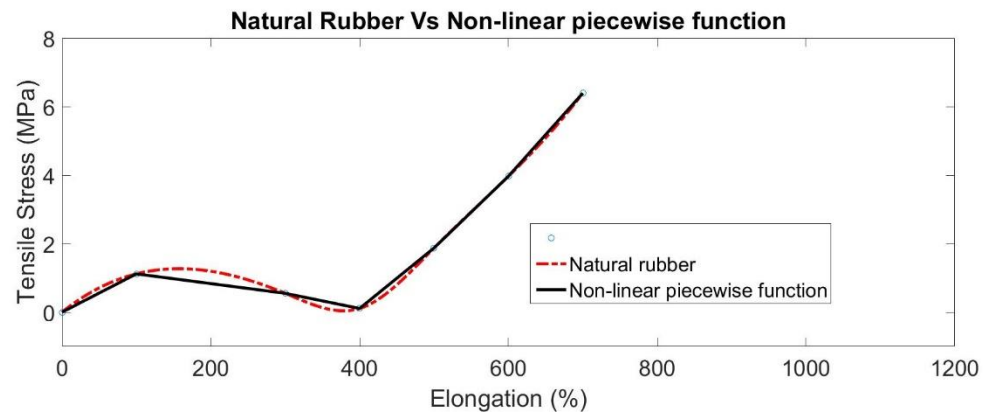
Figure 33 Natural rubber vs piecewise function curve
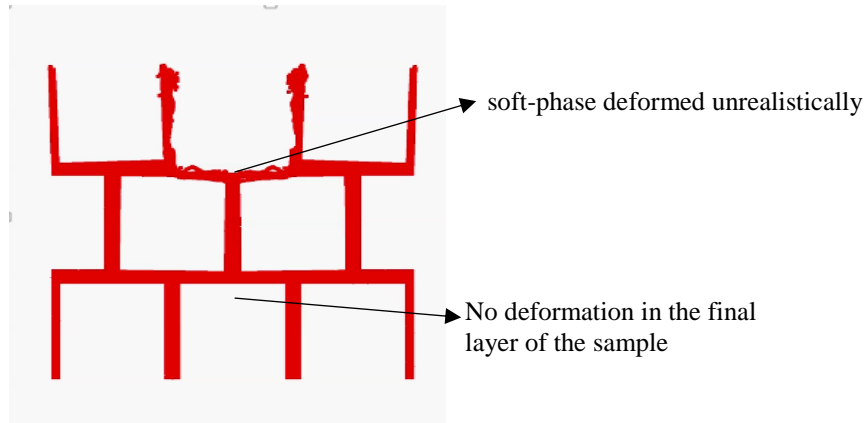


**Figure 34** Soft phase material distribution in 3 brick-mortar structure.
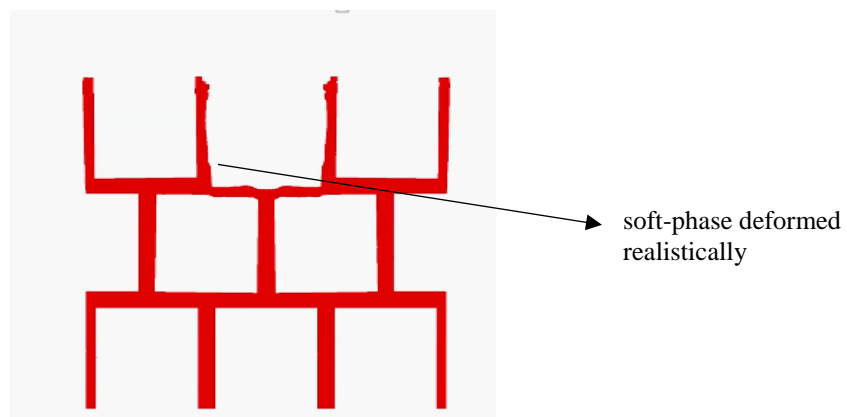


**Figure 35** Non-linear material distribution for the 3-tier brick-mortar model
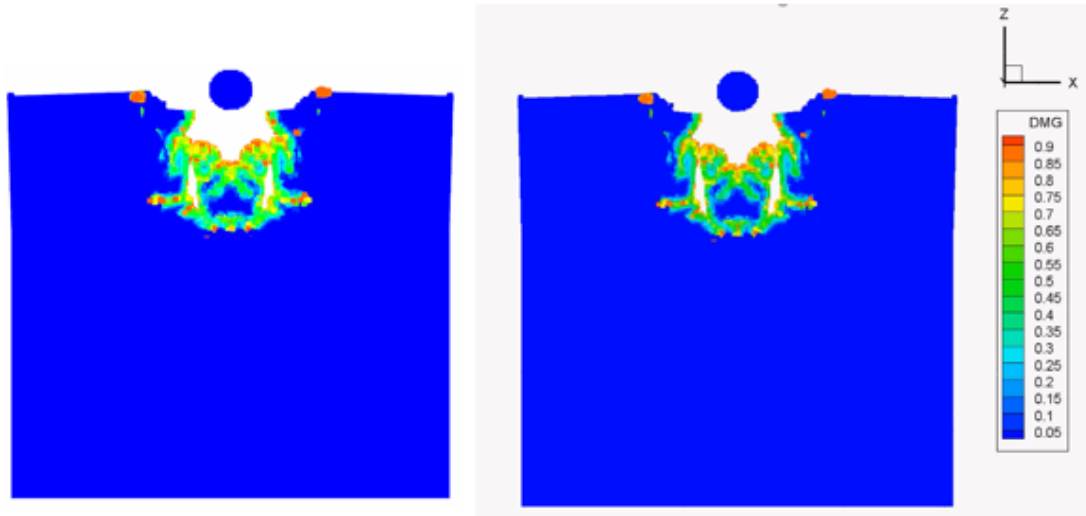
Figure 36 Damage profile for non-linear and linear elastic models on left and right respectively



1 Horizontal Layer

2 Horizontal Layers

2 Horizontal and 2 Vertical Layers

3 Horizontal and 3 Vertical Layers
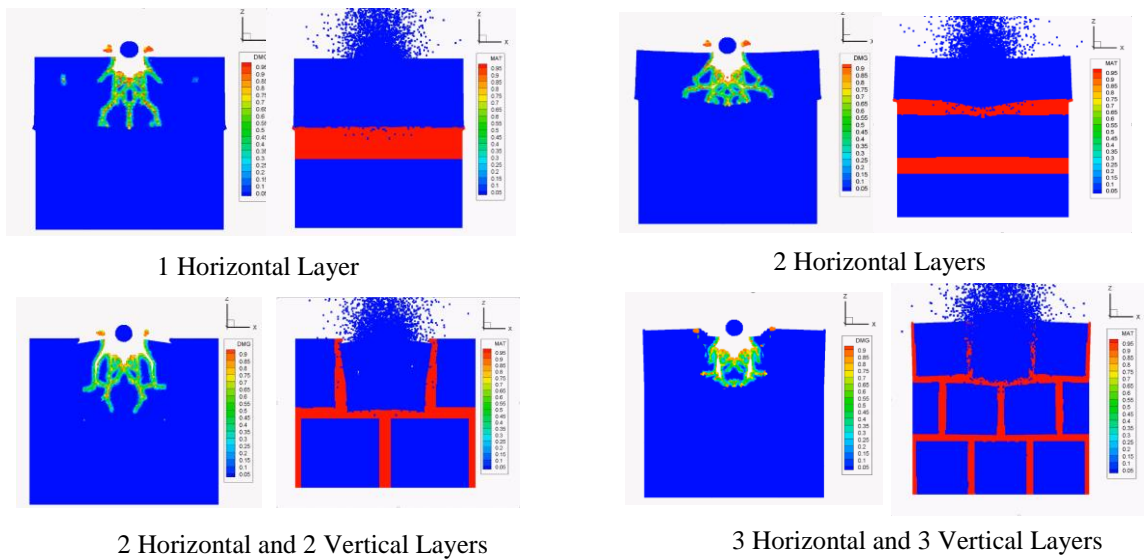
Figure 37  Final Timestep snapshots for different brick-mortar microstructures – damage (columns 1 and 3) and material distribution (columns 2 and 4).

It is observed in all the different microstructures that the damage is limited to the initial stiff phase. The soft phase is observed to have realistic deformation by non-linear elastic model compared to the linearly elastic model.

Upon closer inspection it was found that even with the non-linear model material penetration in the soft phase is observed for the simulations. This has to be addressed in future work. Material penetration exists even with low timestep values as low as 0.1 ns compared to 10 ns scale used for current simulations. The short-range forces were also increased to an order of 1000 times the current value and the material penetration is still observed although a bit less. For example, if the material penetration for current models is seen immediately after one layer of soft phase after lowering the timesteps it is observed after four layers. Thus, these results have to be considered as the preliminary data for future simulations.

# CHAPTER 7:  CONCLUSIONS AND FUTURE WORK

In conclusion, we first selected a brick-mortar microstructure with 20% volume ratio with two stiff and soft phases (VeroClear ,82%, and TangoBlack ,18%). We tested the damage in the brick-mortar sample by low-velocity drop test with two boundary conditions. One boundary condition includes fixing the sample on the steel bed along the direction of impact. Second boundary condition includes the sample to be in the free body without any constraints. It is observed that the damage is seen in the fixed boundary. Cracks are observed at the ends of the sample along with cracks far from the impact. In case of free boundary conditions, the sample did not have damage at these low-velocity impact of drop tower.

A 3D peridynamic dynamic fracture model was created for the brick-mortar structure with a volume ratio of 80% stiff phase and 20% soft phase. Comparing the computational simulations with the experimental results was not successful because of the computational cost. The fixed boundary conditions required modeling of the steel bed which is beyond the computational ability of our lab hence to validate the model we used Kalthoff-Winkler experiments.

Kalthoff-Winkler experiment is a benchmark dynamic fracture problem, with the crack angles of 70 degrees reported. Our computational results were close with measured angles of 66 degrees for the left and 69 degrees for the right notches. After validating our peridynamic model against Kalthoff-Winkler we did convergence studies to determine the horizon size and m for the peridynamic simulations.

With the convergence results, we simulated dynamic impact for a single horizontal layer of the soft phase in stiff phase, two horizontal layers, two-tier brick-mortar and three-tier brick mortar samples. It is observed that the damage in all the cases was limited to the initial brick of impact. We studied soft phase deformation in the sample and observed un-realistic deformation in the three-tier brick-mortar sample. It may be because the soft phase was modeled as a linearly elastic material whereas the rubber (soft phase) is a non-linearly elastic sample. To resolve this a piecewise continuous non-linear model of the soft phase is modeled. After the non-linear soft phase is modeled it is observed that the deformations in the soft phase are smooth and realistic. Damage in both the linear and non-linear cases appears to be same. This indicates that non-linear model helps in seeing the soft phase more clearly, but the damage is represented accurately even with the linear elastic model.

Future work of the thesis includes conducting experiments by high-velocity impact tests with a gas gun with computational inputs for the comparison. The crack propagation in the samples could be captured by a high-speed camera. Parameters of the brick-mortar model such as brick width to length aspect ratio, the volume ratio of soft-stiff phases must be modeled to match the nacre. More microstructures including inclined platelets, helicoidal and Voronoi patterns are to be investigated for the damage. The 3D printing parameters effect of the damage must be studied concerning the plane of build for the samples. Computational simulations have to address material penetration and code should be parallelized to accommodate more layers of soft phase and lower volume ratio of soft phase to hard phase in microstructures.

References

[1] Meyers, M. A., Chen, P., Lin, A. Y., 2008, "Biological Materials: Structure and Mechanical Properties," Progress in Materials Science, **53**(1) pp. 1-206.

[2] Fratzl, P., and Weinkamer, R., 2007, "Nature's Hierarchical Materials," Progress in Materials Science, **52**(8) pp. 1263.

[3] Ulrike G K Wegst, Hao Bai, Eduardo Saiz, 2015, "Bioinspired Structural Materials," Nature Materials, **14**(1) pp. 23-36.

[4] Zengqian Liu a,b, Marc A. Meyers c,d, Zhefeng Zhang b, Robert O. Ritchie a, 2017, "Functional Gradients and Heterogeneities in Biological
Materials: Design Principles, Functions, and Bioinspired
Applications," Progress in Material Science, **88**pp. 467-498.

[5] Barthelat, F. , Rim, J. E. , Espinosa, H. D., 2009, "Applied Scanning Probe Methods XIII,"Springer Berlin Heidelberg, Berlin, Heidelberg, pp. 17-44.

[6] Weaver, J. C., Milliron, G. W., Miserez, A., 2012, "The Stomatopod Dactyl Club: A Formidable Damage-Tolerant Biological Hammer," Science, **336**(6086) pp. 1275.

[7] Jiao, D., Liu, Z. Q., Qu, R. T., 2016, "Anisotropic Mechanical Behaviors and their Structural Dependences of Crossed-Lamellar Structure in a Bivalve Shell," Materials Science & Engineering. C, Materials for Biological Applications, **59**pp. 828-837.

[8] Wegst, U. G., Bai, H., Saiz, E., 2015, "Bioinspired Structural Materials," Nature Materials, **14**(1) pp. 23-36.

[9] Barthelat, F., and Espinosa, H., 2007, "An Experimental Investigation of Deformation and Fracture of Nacre–Mother of Pearl," Experimental Mechanics, **47**(3) pp. 311-324.

[10] Xie, S. S., Vasylkiv, O., Silberschmidt, V., 2013, "Bio-Inspired Structured Boron Carbide-Boron Nitride Composite by Reactive Spark Plasma Sintering," Virtual and Physical Prototyping, **8**(4) pp. 253-258.

[11] Li-Bo Mao, Huai-Ling Gao, Hong-Bin Yao, 2016, "Synthetic Nacre by Predesigned Matrix-Directed Mineralization," Science, **354**(6308) pp. 107-110.

[12] Xiang Gu, G., Su, I., Sharma, S., 2016, "Three-Dimensional-Printing of Bio-Inspired Composites," Journal of Biomechanical Engineering, **138**(2) pp. 16.

[13] Kakisawa, H., Sumitomo, T., Inoue, R., 2010, "Fabrication of Nature-Inspired Bulk Laminar Composites by a Powder Processing," Composites Science and Technology, **70**(1) pp. 161-166.

[14] Wang, K., Chang, Y., Zhang, C., 2016, "Conductive-on-Demand: Tailorable Polyimide/Carbon Nanotube Nanocomposite Thin Film by Dual-Material Aerosol Jet Printing," Carbon, **98**pp. 397-403.

[15] Salinas, C. L., de Obaldia, E. E., Jeong, C., 2017, "Enhanced Toughening of the Crossed Lamellar Structure Revealed by Nanoindentation," Journal of the Mechanical Behavior of Biomedical Materials, **76**pp. 58-68.

[16] Knipprath, C., Bond, I. P., and Trask, R. S., 2012, "Biologically Inspired Crack Delocalization in a High Strain-Rate Environment," Journal of the Royal Society, Interface / the Royal Society, **9**(69) pp. 665-676.

[17] Dimas, L.S., 2013, "Bio-inspired Composites, a de novo Approach to the Conceptualization, Design and Synthesis of Tough Mesoscale Structures with Simple Building Blocks," .

[18] Djumas, L., Molotnikov, A., Simon, G. P., 2016, "Enhanced Mechanical Performance of Bio-Inspired Hybrid Structures Utilising Topological Interlocking Geometry," Scientific Reports, **6**pp. 26706.

[19] Theresa Swetly, Jürgen Stampfl, Gero Kempf, 2016, "Bioinspired Engineering Polymers by Voxel-Based 3D-Printing," BioNanoMaterials, **17**(3) pp. 145-157.

[20] Challis, V., Roberts, A., and Wilkins, A., 2008, "Fracture Resistance Via Topology Optimization," Structural and Multidisciplinary Optimization, **36**(3) pp. 263-271.

[21] Das, R., Jones, R., and Xie, Y. M., 2005, "Design of Structures for Optimal Static Strength using ESO," Engineering Failure Analysis, **12**(1) pp. 61-80.

[22] Gu, G. X., Dimas, L., Qin, Z., 2016, "Optimization of Composite Fracture Properties: Method, Validation, and Applications," Journal of Applied Mechanics, **83**(7) pp. 7.

[23] James, K. A., and Waisman, H., 2015, "Topology Optimization of Structures Under Variable Loading using a Damage Superposition Approach," International Journal for Numerical Methods in Engineering, **101**(5) pp. 375-406.

[24] Dimas, L.S., 2013, "Bio-inspired Composites, a de novo Approach to the Conceptualization, Design and Synthesis of Tough Mesoscale Structures with Simple Building Blocks," .

[25] Ganesan, Y., Peng, C., Lu, Y., 2011, "Interface Toughness of Carbon Nanotube Reinforced Epoxy Composites," ACS Applied Materials & Interfaces, **3**(2) pp. 129.

[26] Yao, Y., Zeng, X., Sun, R., 2016, "Highly Thermally Conductive Composite Papers Prepared Based on the Thought of Bioinspired Engineering," ACS Applied Materials & Interfaces, **8**(24) pp. 15645.

[27] Begley, M. R., Philips, N. R., Compton, B. G., 2012, "Micromechanical Models to Guide the Development of Synthetic 'brick and Mortar' Composites," Journal of the Mechanics and Physics of Solids, **60**(8) pp. 1545.

[28] Zhang, C., Mcadams, D. A., and Grunlan, J. C., 2016, "Nano/Micro-Manufacturing of Bioinspired Materials: A Review of Methods to Mimic Natural Structures," Advanced Materials, **28**(30) pp. 6292-6321.

[29] Ginzburg, D., Pinto, F., Iervolino, O., 2017, "Damage Tolerance of Bio-Inspired Helicoidal Composites Under Low Velocity Impact," Composite Structures, **161**pp. 187-203.

[30] Dutta, A., Vanderklok, A., and Tekalur, S. A., 2012, "High Strain Rate Mechanical Behavior of Seashell-Mimetic Composites: Analytical Model Formulation and Validation," Mechanics of Materials, **55**pp. 102-111.

[31] Theresa Swetly, Jürgen Stampfl, Gero Kempf, 2016, "Bioinspired Engineering Polymers by Voxel-Based 3D-Printing," BioNanoMaterials, **17**(3) pp. 145-157.

[32] Michael W. Barclift, and Christopher B. Williams Design, "Examining Variability in the Mechanical Properties of Parts Manufactured Via Polyjet Direct 3d Printing," .

[33] Silling, S. A., 2000, "Reformulation of Elasticity Theory for Discontinuities and Long-Range Forces," Journal of the Mechanics and Physics of Solids, **48**(1) pp. 175-209.

[34] Silling, S. A., and Askari, E., 2005, "A Meshfree Method Based on the Peridynamic Model of Solid Mechanics," Computers and Structures, **83**(17) pp. 1526-1535.

[35] Silling, S.A., and Lehoucq, R.B., 2010, "Advances in Applied Mechanics,"Elsevier Science & Technology, pp. 73-168.

[36] J. Mehrmashhadi, Y. Tang, X. Zhao, Z. Xu, J. Pan, and Q. V. Le, 2018, "The Effect of Solder Joint Microstructure on the Drop Test Failure: A Peridynamic Analysis," IEEE Trans. Compon. Packag. Manuf. Technol., .

[37] Silling, S. A., Gerstle, W. H., and Sau, N., Aug 1, 2005, "Peridynamic modeling of plain and reinforced concrete structures," Anonymous USDOE, United States, .

[38] Oterkus, S., Madenci, E., and Agwai, A., 2014, "Peridynamic Thermal Diffusion," Journal of Computational Physics, **265**pp. 71-96.

[39] Madenci, E., and Oterkus, E., 2014, "Peridynamic Theory and Its Applications," Springer New York, New York, NY, .

[40] Macek, R. W., and Silling, S. A., 2007, "Peridynamics Via Finite Element Analysis," Finite Elements in Analysis & Design, **43**(15) pp. 1169-1178.

[41] Kalthoff, J. F., and Winkler, S., 1988, "Failure Mode Transition at High Rates of Shear Loading," Impact Loading and Dynamic Behavior of Materials, **1**pp. 185-195.

[42] Needleman, A., and Tvergaard, V., 1995, "Analysis of a Brittle-Ductile Transition Under Dynamic Shear Loading," International Journal of Solids and Structures, **32**(17) pp. 2571-2590.

[43] Zhou, M., Rosakis, A. J., and Ravichandran, G., 1996, "Dynamically Propagating Shear Bands in Impact-Loaded Prenotched plates—I. Experimental Investigations of Temperature Signatures and Propagation Speed," Journal of the Mechanics and Physics of Solids, **44**(6) pp. 981-1006.

[44] Belytschko, T., Chen, H., Xu, J., 2003, "Dynamic Crack Propagation Based on Loss of Hyperbolicity and a New Discontinuous Enrichment," International Journal for Numerical Methods in Engineering, **58**(12) pp. 1873-1905.

[45] Nguyen, V. P., 2014, "Discontinuous Galerkin/Extrinsic Cohesive Zone Modeling: Implementation Caveats and Applications in Computational Fracture Mechanics," Engineering Fracture Mechanics, **127**pp. 37.

[46] Park, K., Paulino, G. H., Celes, W., 2012, "Adaptive Mesh Refinement and Coarsening for Cohesive Zone Modeling of Dynamic Fracture," International Journal for Numerical Methods in Engineering, **92**(1) pp. 1-35.

[47] Russell Thomas Hollman, 2017, "Mixed-Mode Dynamic Crack Propagation using the Discontinuous Galerkin Method," pp. 1-52.

[48] Raymond, S., Lemiale, V., Ibrahim, R., 2014, "A Meshfree Study of the Kalthoff-Winkler Experiment in 3D at Room and Low Temperatures Under Dynamic Loading using Viscoplastic Modelling," Engineering Analysis with Boundary Elements, **42**pp. 20.

[49] Ean Tat Ooi a, Sundararajan Natarajan , Chongmin Song , Ean Hin Ooi, 2016, "Dynamic Fracture Simulations using the Scaled Boundary Finite
Element Method on Hybrid Polygon–quadtree Meshes," (International Journal of Impact Engineering) pp. 154-164.

[50] Wildman, R., O'Grady, J., and Gazonas, G., 2017, "A Hybrid Multiscale Finite Element/Peridynamics Method," International Journal of Fracture, **207**(1) pp. 41-53.

[51] Gu, X., Zhang, Q., and Xia, X., 2017, "Voronoi-based Peridynamics and Cracking Analysis with Adaptive Refinement," International Journal for Numerical Methods in Engineering, **112**(13) pp. 2087-2109.

[52] Silling, S.A., 2003, "Computational Fluid and Solid Mechanics 2003,"Elsevier Science Ltd, pp. 641-644.

[53] Ren, H., Zhuang, X., and Rabczuk, T., 2017, "Dual-Horizon Peridynamics: A Stable Solution to Varying Horizons," Computer Methods in Applied Mechanics and Engineering, .

[54] Dipasquale, D., Zaccariotto, M., and Galvanetto, U., 2014, "Crack Propagation with Adaptive Grid Refinement in 2D Peridynamics," International Journal of Fracture, **190**(1) pp. 1-22.

[55] Ren, H., Zhuang, X., Cai, Y., 2016, "Dual-horizon Peridynamics," International Journal for Numerical Methods in Engineering, **108**(12) pp. 1451-1476.

[56] Bobaru, F., Yang, M., Alves, L. F., 2009, "Convergence, Adaptive Refinement, and Scaling in 1D Peridynamics," International Journal for Numerical Methods in Engineering, **77**(6) pp. 852-877.

[57] Ha, Y. D., and Bobaru, F., 2010, "Studies of Dynamic Crack Propagation and Crack Branching with Peridynamics," International Journal of Fracture, **162**(1-2) pp. 229-244.

[58] Polyurethane products, "Engineering Information- Natural Rubber," .